



# LUND UNIVERSITY

## Surface structure and catalytic activity of Pd and Fe oxide surfaces and thin films

Shipilin, Mikhail

2016

*Document Version:*

Publisher's PDF, also known as Version of record

[Link to publication](#)

*Citation for published version (APA):*

Shipilin, M. (2016). *Surface structure and catalytic activity of Pd and Fe oxide surfaces and thin films*. [Doctoral Thesis (compilation), Faculty of Science]. Lund University, Faculty of Science, Department of Physics, Division of Synchrotron Radiation Research.

*Total number of authors:*

1

### General rights

Unless other specific re-use rights are stated the following general rights apply:

Copyright and moral rights for the publications made accessible in the public portal are retained by the authors and/or other copyright owners and it is a condition of accessing publications that users recognise and abide by the legal requirements associated with these rights.

- Users may download and print one copy of any publication from the public portal for the purpose of private study or research.
- You may not further distribute the material or use it for any profit-making activity or commercial gain
- You may freely distribute the URL identifying the publication in the public portal

Read more about Creative commons licenses: <https://creativecommons.org/licenses/>

### Take down policy

If you believe that this document breaches copyright please contact us providing details, and we will remove access to the work immediately and investigate your claim.

LUND UNIVERSITY

PO Box 117  
221 00 Lund  
+46 46-222 00 00

# Surface structure and catalytic activity of Pd and Fe oxide surfaces and thin films

by Mikhail Shipilin

Division of Synchrotron Radiation Research



**LUND**  
UNIVERSITY

DOCTORAL DISSERTATION

Cover illustration front: “Happy frog”. An integrated HESXRD scan of a faceted Pd(110) surface.

Doctoral dissertation  
Division of Synchrotron Radiation Research  
Department of Physics  
Lund University

© Mikhail Shipilin 2016  
ISBN: 978-91-7623-967-4 (print)  
ISBN: 978-91-7623-968-1 (pdf)

Printed in Sweden by Media-Tryck, Lund University, Lund 2016



*Dedicated to my wife and parents.*



## Abstract

The present work is devoted to atomic scale structural studies of the surfaces of model heterogeneous catalysts relevant to oxidation reactions. A novel approach using high-energy surface X-ray diffraction combined with mass-spectrometry measurements is employed to perform *in situ* structural characterization of Pd(100) and Pd(553) single crystal surfaces acting as catalysts in the process of CO oxidation under semirealistic conditions. The experimental approach greatly facilitates the understanding of surface X-ray diffraction and improves significantly the data collection speed. The phases forming on the surfaces in gas mixtures with different relative concentrations of CO and O<sub>2</sub> are determined and are associated to the catalytic activity. The corresponding structural models are proposed.

A combination of complementary experimental techniques, including conventional surface X-ray diffraction, X-ray photoelectron spectroscopy, Auger electron spectroscopy, low-energy electron diffraction, scanning tunneling microscopy, temperature programmed desorption spectroscopy and reflection absorption infrared spectroscopy as well as theoretical calculations, is employed to study in detail the structural and NO adsorption properties of iron oxide ultrathin films grown on Ag(100) and Ag(111) single crystal substrates. Structural models of different phases growing on the surfaces under different preparation conditions are presented. The atomic structural model of a one-layer thick FeO(111) film grown on Ag(100) is proposed. The NO adsorption properties of one-layer thick FeO(111) films on both substrates are investigated and compared to the NO adsorption properties of FeO(111)/Pt(111) reported in the literature. The observed differences are discussed in detail.

The results obtained for CO oxidation over Pd model catalysts allow for an increased understanding of the processes occurring on the surface of a working catalyst and the connection between the catalytic properties and the surface structure. The performed studies of iron oxide ultrathin films grown on silver substrates provide insight into how the structural properties are related to the adsorption properties of such systems and knowledge important for the design of novel catalytic materials with improved qualities.



## Popular Science Summary

Catalytic processes have tremendous importance in our everyday life. Most chemicals, pharmaceuticals, plastics etc. are, in fact, produced with the help of catalysts. What is probably even more important is that the toxic wastes produced in great amounts by modern factories and plants are recycled or transformed into less poisonous substances by means of catalytic units. One example from our everyday life is the exhaust of car engines and toxic emission of power plants. The products of fuel combustion, e.g. carbon monoxide, are extremely harmful for our health and environment. In order to reduce the negative impact, cleaning systems containing catalytically active materials are employed to handle toxic compounds.

The reason why we need catalysts to transform one gas into another is that not all processes are favorable in nature and not all of them can proceed on their own. To continue with the carbon monoxide gas example, when the molecules of CO and the molecules of O<sub>2</sub> are trapped together in a confined volume, they will simply coexist in a mixture preserving their identity. They do not react with each other because of the lack of energy required to initiate the reaction. The picture changes if a catalytically active material, e.g. platinum or palladium is introduced in the system. The gas molecules can then attach to the surface, where due to the interaction of electrons between the molecules and the substrate atoms, they can be activated and react with each other to produce CO<sub>2</sub>. This process is called heterogeneous catalysis because a solid catalyst is participating in the reaction of gases.

Since heterogeneous catalytic reactions occur on the surface of a catalyst, it is clear that in order to handle greater amount of gases a more extended surface area is necessary. To achieve this, small particles of a catalytically active material, which all together have a much larger surface area than any extended bulk form, are deposited on a porous substrate, which is enclosed in a vessel attached to the emission line. Such catalytic units are widely produced and available for industrial use. In order to develop new, better and cheaper catalysts, however, the studies of the processes occurring on the surface of the active material are necessary. In particular, it is important to determine the atomic structure and its influence on the chemical and physical properties of the surface of the particles.

The present dissertation reports on research work aimed at understanding the connection between structural properties of model catalysts and their catalytic performance. The samples used in the studies are extended atomically flat surfaces of crystals and thin films grown on them. The use of model catalysts is a way to overcome one of the two main problems arising in surface science – the *material gap* (between industrial catalysis and laboratory studies). It appears due to a restricted access to the particles in a real catalytic units. The second – the *pressure gap* – is constituted by the inability of most surface sensitive experimental techniques to operate under atmospheric pressures and, as a result, the requirement

of ultra high vacuum conditions in an experiment. In the current work we employ a novel technique based on X-ray radiation, which can overcome the pressure restriction.

The results reported in the dissertation show that when the surface of Pd acts as a catalyst in CO oxidation, a one-layer thick Pd oxide film forms on the surface and it is this compound that actually promotes the reaction. This film grows in thickness and finally loses the high degree of structural order upon increase of oxygen concentration. A stepped surface of Pd was also studied in a similar way in order to increase the complexity of the model system and approach closer to real catalysts. The steps on the surface mimic the edges of catalyst particles to a certain extent and allow to study the way they affect the reaction.

Another model system studied in the current work is thin iron oxide films grown on Ag substrates. They were shown to perform well in catalytic oxidation processes. The reported results are therefore important for understanding of the catalytic performance of the studied structures. The special feature of such thin films is that, due to the difference between their atomic arrangement and that of the substrate, they can form completely different two-dimensional structures with different properties depending on the particular substrate and preparation conditions. The results of the current studies deliver insight into this dependence, which is necessary for the design of novel functional two-dimensional materials with desired properties.

## Preface

This dissertation is based on the following publications, referred to by their Roman numerals:

### **I – High-Energy Surface X-ray Diffraction for Fast Surface Structure Determination**

J. Gustafson, M. Shipilin, C. Zhang, A. Stierle, U. Hejral, U. Ruett, O. Gutowski, P.-A. Carlsson, M. Skoglundh, E. Lundgren  
Science 343(6172), pp. 758-761, 2014. DOI: 10.1126/science.1246834

*I performed much of the experimental work as well as data analysis. I wrote a computer code that allowed to extract the quantitative data from the experiments, and fitted the experimental data to structural models.*

### **II – Quantitative Surface Structure Determination Using In Situ High-Energy SXRD: Surface Oxide Formation on Pd(100) During Catalytic CO Oxidation**

M. Shipilin, U. Hejral, E. Lundgren, L. R. Merte, C. Zhang, A. Stierle, U. Ruett, O. Gutowski, M. Skoglundh, P.-A. Carlsson, J. Gustafson  
Surf. Sci. 630, pp. 229-235, 2014. DOI: 10.1016/j.susc.2014.08.021

*I performed much of the experimental work as well as data analysis. I extracted the quantitative data from the experiments, and fitted the experimental data to structural models. I was the main responsible for the writing and submitted the manuscript.*

### **III – The Influence of Incommensurability on the Long Range periodicity of the Pd(100)-( $\sqrt{5} \times \sqrt{5}$ )R27°-PdO(101)**

M. Shipilin, J. Gustafson, L. R. Merte, A. Stierle, U. Hejral, N. M. Martin, C. Zhang, E. Lundgren  
In manuscript

*I performed much of the experimental work. I extracted the quantitative data from the experiments, and did a detailed analysis. I was the main responsible for the writing of the manuscript.*

### **IV – Transient Structures of PdO During CO Oxidation Over Pd(100)**

M. Shipilin, J. Gustafson, C. Zhang, L. R. Merte, A. Stierle, U. Hejral, U. Ruett, O. Gutowski, M. Skoglundh, P.-A. Carlsson, E. Lundgren  
J. Phys. Chem. C 119(27), pp. 15469-15476, 2015. DOI: 10.1021/acs.jpcc.5b04400

*I performed much of the experimental work as well as data analysis. I extracted the quantitative*

*data from the experiments, and fitted the experimental data to structural models. I was the main responsible for the process of writing and submitting of the manuscript.*

## **V – Step Dynamics and Oxide Formation During CO Oxidation over a Vicinal Pd Surface**

**M. Shipilin**, J. Gustafson, C. Zhang, L. R. Merte, E. Lundgren

Phys. Chem. Chem. Phys. 18, pp. 20312-20320, 2016. DOI: 10.1039/c5cp07488f

*I performed much of the experimental work as well as data analysis. I extracted the quantitative data from the experiments, and fitted the experimental data to structural models. I was the main responsible for the writing and the submitting of the manuscript.*

## **VI – Growth of Ultrathin Iron Oxide Films on Ag(100)**

L. R. Merte, **M. Shipilin**, S. Ataran, S. Blomberg, C. Zhang, A. Mikkelsen, J. Gustafson, E. Lundgren

J. Phys. Chem. C 119(5), pp. 2572-2582, 2015. DOI: 10.1021/jp511496w

*I participated in the experiments and supported the manuscript writing and the discussion.*

## **VII – Fe Oxides on Ag Surfaces: Structure and Reactivity**

**M. Shipilin**, E. Lundgren, J. Gustafson, C. Zhang, F. Bertram, C. Nicklin, C. J. Heard, H. Grönbeck, F. Zhang, J. Choi, V. Mehar, V. J. F. Weaver, L. R. Merte

Topics in Catalysis: Surface Chemistry of Well-Characterized Metal Oxides, 2016. DOI: 10.1007/s11244-016-0714-8

*I performed a great part of the reported experimental measurements, fitted the data and proposed the structural model. I was the main responsible for the writing and submitted the manuscript.*

## **VIII – Adsorption of NO on FeO<sub>x</sub> Films Grown on Ag(111)**

V. Mehar, L. R. Merte, J. Choi, **M. Shipilin**, E. Lundgren, J. F. Weaver

J. Phys. Chem. C 120(17), pp. 9282-9291, 2016. DOI: 10.1021/acs.jpcc.6b01751

*I participated in the experiments and supported the manuscript writing and the discussion.*

## **IX – Tuning the Reactivity of Ultrathin Oxides: NO Adsorption on Monolayer FeO(111)**

L. R. Merte, C. J. Heard, F. Zhang, J. Choi, **M. Shipilin**, J. Gustafson, J. F. Weaver, H. Grönbeck, E. Lundgren

Angew. Chem. Int. Ed. 55(32), pp. 9267-9271, 2016. DOI: 10.1002/anie.201601647

*I participated in the experiments and supported the manuscript writing and the discussion.*

Publications related but not included in the present dissertation:

**Faceting of Rhodium(553) in Realistic Reaction Mixtures of Carbon Monoxide and Oxygen**

C. Zhang, E. Lundgren, P.-A. Carlsson, O. Balmes, A. Hellman, L. R. Merte, **M. Shipilin**, W. Onderwaater, J. Gustafson  
J. Phys. Chem. C 119(21), pp. 11646-11652, 2015. DOI: 10.1021/acs.jpcc.5b01841

**X-ray Photoemission Analysis of Clean and Carbon Monoxide-Chemisorbed Platinum(111) Stepped Surfaces Using a Curved Crystal**

A. L. Walter, F. Schiller, M. Corso, L. R. Merte, F. Bertram, J. Lobo-Checa, **M. Shipilin**, J. Gustafson, E. Lundgren, A. X. Brion-Rios, P. Cabrera-Sanfeliix, D. Sanchez-Portal, J. E. Ortega  
Nat. Commun. 6, pp. 8903-1-7, 2015. DOI: 10.1038/ncomms9903

**The Thickness of Native Oxides on Aluminum Alloys and Single Crystals**

J. Evertsson, F. Bertram, F. Zhang, L. Rullik, L. R. Merte, **M. Shipilin**, M. Soldemo, S. Ahmadi, N. Vinogradov, F. Carla, J. Weissenrieder, M. Göthelid, J. Pan, A. Mikkelsen, J.-O. Nilsson, E. Lundgren  
Appl. Surf. Sci. 349, pp. 826-832, 2015. DOI: 10.1016/j.apsusc.2015.05.043



## Abbreviations

AES	Auger Electron Spectroscopy
AFM	Atomic Force Microscopy
BCC	Body-Centered Cubic
CTR	Crystal Truncation Rod
DFT	Density Functional Theory
FCC	Face-Centered Cubic
(HE)SXR	(High-Energy) Surface X-Ray Diffraction
IMFP	Inelastic Mean Free Path
LDOS	Local Density Of States
LEED	Low-Energy Electron Diffraction
QMS	Quadrupole Mass Spectrometer/Spectroscopy
RAIRS	Reflection Absorption InfraRed Spectroscopy
SC	Simple Cubic
SR	Superstructure Rod
STM	Scanning Tunneling Microscopy
TPD	Temperature Programmed Desorption
UHV	Ultra-High Vacuum
XPS	X-ray Photoelectron Spectroscopy
XRD	X-Ray Diffraction



## Acknowledgments

The period of doctoral studies is both exciting and difficult. Depending on people around, one can have more of the first or more of the second. I was utterly lucky in this sense and had the best working conditions one could wish for. Here I will try to acknowledge and thank all people who helped me in one or another way. They all made a great contribution in my work and life and, regardless of the order in which I mention them, made my achievements possible.

First of all, I would like to thank my supervisor Prof. **Edvin Lundgren**. I'm indebted to him enormously for everything he did for me from the very beginning, when I was invited for the interview and later was accepted as a doctoral student, to the present moment. I thank Edvin for his professional qualities that helped me to realize what a scientist should be: intelligent, erudite, always curious and ready to try new ideas. I am grateful for his infinite patience, understanding and kindness. In a major part it was Edvin who motivated me and made my studies and work exciting, meaningful and fruitful.

Another person, without whom I would not be able to come to the finish line, is my co-supervisor Dr. **Johan Gustafson**. Many experiments were done with his guidance and help, many discussions resulted in new ideas and interpretations. I thank Johan for the possibility to ask any question at any time and his friendly help with any problem that was arising during my work on the project. His intelligence in physics and broad skills in everything from computer programming to paper writing is something that again and again impresses me.

I would like to thank my colleague and friend Dr. **Lindsay Merte**, with whom I was often working side by side, for the stimulating discussions, his insightful comments and constant encouragement. His outstanding professionalism and immense knowledge along with the persistence in achieving goals always motivated me. Not only scientific work we shared but also free time, the memories of which will always remain with me.

I thank Dr. **Andreas Schaefer** who has a unique combination of high professionalism and humor. Except being one of the smartest people I've ever met, Andreas showed me that science is actually fun, that chocolate is essential during a beamtime, that liquid nitrogen makes funny patterns if poured in a cup of coffee and many other things I will remember for a long time.

I thank my colleague and friend Dr. **Uta Hejral** for the sleepless nights we were working together during our experiments and for all the fun we had in between.

My sincere thanks also go to my close colleagues Dr. **Natalia Martin** for valuable advices and the help with experiments, **Chu Zhang**, **Sara Blomberg** and **Jonas Evertsson** for the excellent cooperation, which resulted in several high-quality publications.

An important part of the work that was done during the last four years would not be possible to perform without people working at different places, where the experiments were taking place. I would like to thank Prof. **Andreas Stierle** for valuable discussions and the members of his research group Dr. **Dirk Franz**, Dr. **Vedran Vonk** and **Patrick Müller** for their help and support. An invaluable help of Dr. **Uta Ruett** and **Olof Gutowski** at the P07 beamline of the Petra III synchrotron made it possible for me to start understanding surface X-ray diffraction principles. I'm grateful to Dr. **Per-Anders Carlsson** and Prof. **Magnus Skoglundh** for their help in the experiments. I appreciate the collaboration with the combustion physics crew – Dr. **Johan Zetterberg**, **Jianfeng Zhou** and **Sebastian Pfaff** – who made it possible to perform very interesting experiments combining PLIF and HESXRD. I would also like to thank Prof. **Jason Weaver** and the members of his group at the University of Florida, **Vikram Mehar** and **Juhee Choi**, for their help with experimental work and publishing the obtained results.

I am grateful to my colleagues and friends Dr. **Estephania Lira** and Dr. **Sarah Mckibbin** for interesting lunch time discussions and great free time spent together.

I would like to thank all people working at the Division of Synchrotron Radiation Research at Lund University for the warm and friendly ambiance at the place where I worked. Special thanks go to **Patrik Wirgin**, who was always incredibly helpful with all formalities and paperwork making life much easier.

I am immensely grateful to the people, who were not directly involved in my scientific work but nevertheless contributed greatly to my successes and softened my failures – my friends. These special thanks go to **Maksim Isaev**, **Grigory Arutsev**, **Benjamin Tallmadge**, **Elisabetta Rosso**, **Nicholai Mauritzsson**, Dr. **Mikhail Kondrashov**, **Jevgenij Aleksandrov**, **Irina Timoshenko**, **Vladimir Pastukhov**, Dr. **Konstantin Simonov**, Dr. **Nikolay Vinogradov**, **Maria Ruchkina**.

The greatest regards go to my family – my wife **Maria Shipilina**, and my parents **Anatoly Shipilin** and **Irina Zakharova**. It is they, who fill my life with meaning and support me like nobody else in any situation.

# Contents

Abstract . . . . .	vii
Popular Science Summary . . . . .	ix
Preface . . . . .	xi
Abbreviations . . . . .	xv
Acknowledgments . . . . .	xvii
<b>Introduction</b>	<b>1</b>
<b>1 Crystal Structure</b>	<b>7</b>
1.1 Crystal lattices . . . . .	7
1.2 Crystalline materials . . . . .	9
1.3 Crystal surfaces . . . . .	10
<b>2 Heterogeneous Catalysis</b>	<b>13</b>
2.1 Gas-surface interactions . . . . .	13
2.2 CO oxidation . . . . .	15
<b>3 Surface Oxides and Thin Oxide Films</b>	<b>17</b>
3.1 Surface oxidation . . . . .	17
3.2 Thin films . . . . .	19
<b>4 Investigation of Surfaces</b>	<b>21</b>
4.1 X-ray diffraction from single crystal surfaces . . . . .	21
4.1.1 X-ray diffraction basics . . . . .	22
4.1.2 X-ray diffraction from surfaces . . . . .	28
4.1.3 Surface X-ray diffraction . . . . .	29
4.1.4 Synchrotron radiation and beamlines . . . . .	33
4.2 Low-energy electron diffraction . . . . .	34
4.3 Scanning tunneling microscopy . . . . .	38
4.4 Spectroscopy . . . . .	41
4.4.1 X-ray photoelectron spectroscopy . . . . .	42
4.4.2 Auger electron spectroscopy . . . . .	44
4.4.3 Reflection absorption infrared spectroscopy . . . . .	45
4.4.4 Temperature programmed desorption spectroscopy . . . . .	47
4.5 Theoretical calculations . . . . .	49

4.5.1	Density functional theory . . . . .	49
4.5.2	STM simulation . . . . .	50
	<b>Summary of Papers</b>	<b>51</b>
	<b>Conclusions and Outlook</b>	<b>55</b>
	<b>Bibliography</b>	<b>57</b>

# Introduction

It is difficult to overestimate the importance of catalysts for modern society. To give some examples, most industrially produced inorganic chemicals, plastics and pharmaceuticals, which are part of our everyday life, would be almost impossible to make in a non-catalytic way. Less visible but maybe even more important processes of, e.g. exhaust gas cleaning or ammonia synthesis would as well fail without catalysis. An increased understanding of the principals of catalytic processes is therefore expected to promote more efficient approaches, including the design and development of new catalytic materials. Therefore the scientific quest in the field of catalysis, that started almost two centuries ago and has been enormously expanding with time, is far from the end and demands more efforts.

The first to coin the name for the phenomenon of catalysis was the Swedish chemist Jöns Jacob Berzelius, who in 1836 published a review of existing observations indicating that certain substances influence chemical processes without being affected by the reactions [1, 2]. The description was however rather vague until about 1901 when the Russian-German chemist Wilhelm Ostwald proposed the definition of catalysis that is still valid today: “*A catalyst is a substance which affects the rate of a chemical reaction without being part of its end products*” [3].

The basic principle behind catalysis is that the presence of a catalyst allows for certain intermediate steps of a chemical reaction. All together, they are more energetically favorable than a direct path from the reactants to the products without a catalyst (see in Figure I1). The energy barrier of each step of a catalyzed reaction is often much lower than the barrier of a direct non-catalyzed path making the reaction rate significantly higher. However, catalysts influence only the kinetics of a reaction but not its thermodynamics, which means that if the products are thermodynamically unstable the reaction is still prohibited.

Catalysts can have different forms and various mechanisms of interaction with reactants. In heterogeneous catalysis, the catalyst and the reacting substance are, as suggested by the name, in different states, e.g. a solid catalyst and gaseous reactants. In such a combination, the surface of the solid serves as the playground for the reaction, where gas molecules adsorb, become activated, react and desorb. The canonic example of a heterogeneous catalytic

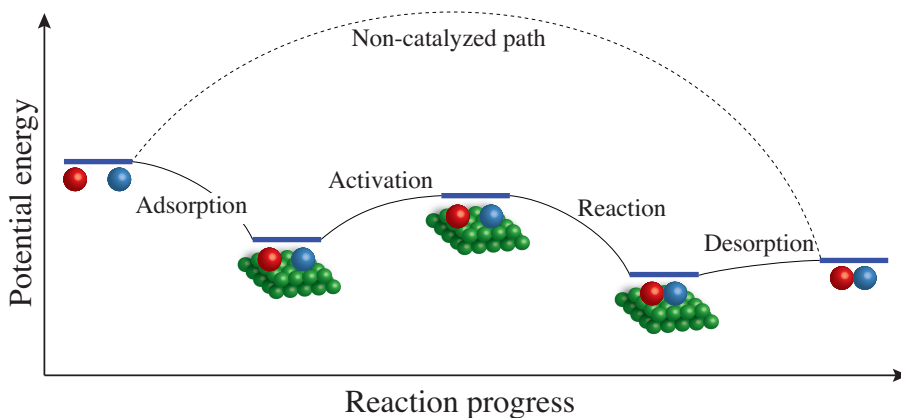
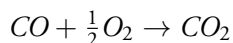


Figure I1: A schematic view of direct and catalyzed paths of a reaction.

process is carbon monoxide oxidation [4], a reaction studied extensively in the present dissertation. This gas, emitted as a side product of many combustion reactions, e.g. in power plants or vehicle engines, is highly toxic and harmful for human health and the environment. In order to reduce the negative impact of carbon monoxide, it can be converted into less harmful carbon dioxide according to the following reaction scheme



The difficulty lies in the fact that this reaction cannot proceed efficiently in the gas phase under regular conditions and requires the presence of a catalyst [5, 6].

Industrial catalysts handling gases are usually fabricated of a porous material with dispersed nanoparticles of an active element or compound. Since nanoparticles have a high surface to bulk ratio, it allows for the largest possible effective area with relatively small amount of material. The latter is important because in many cases rare and valuable elements are used as the active agent. In Figure I2 the structure of a catalyst for the reaction of carbon monoxide oxidation is schematically shown.

Since catalytic reactions occur on the surface of a solid catalyst, it is important to understand the interaction of molecules with the crystal surface to achieve a better understanding of catalytic mechanisms. Unlike the atoms in the bulk of a solid, the surface atoms are lacking a part of their neighbors and, as a result, a part of their atomic bonds. This leads to a distinct electronic configuration of surface atoms and consequently to special and unique physical and chemical properties of the surface. In experimental work, the contribution of the outermost atomic layer may easily be negligible when studying a solid by means of experimental techniques that are not specifically surface sensitive. This fact should always be kept in mind when studying solid catalysts [7] since catalytic reactions happen on the

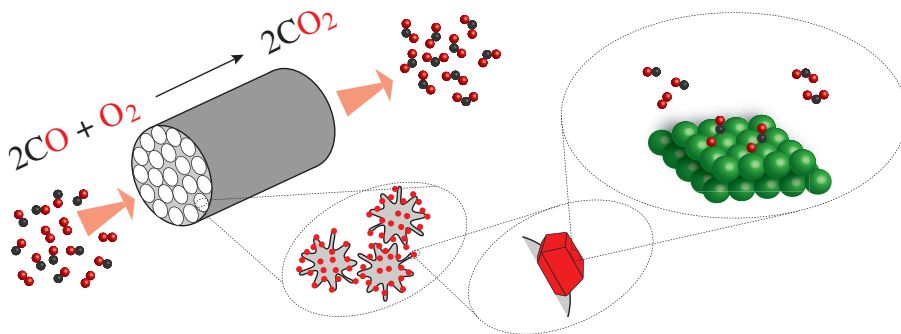


Figure I2: A schematic view of a working heterogeneous catalyst. From left to right the scale decreases.

surface.

The macroscopic structure of a real applied catalyst makes it difficult to interrogate the surface of the active material with most measuring techniques – this complication is known as the *material gap*. Therefore, simplified structures mimicking the facets of catalytically active nanoparticles are widely used as model systems in studies of the interaction between reactants and the surface of a catalyst. A good example is the surface of a single crystal acting as a catalyst in a particular chemical reaction. Single crystal surfaces expose a well defined atomic arrangement that can be relatively easily accessed. Another common problem known as the *pressure gap* is caused by the fact that many surface sensitive techniques can not be applied under atmospheric pressure, which usually exists in a real applied catalyst. This happens because it is common to employ electrons as the surface probe as they have a short mean free path and don't penetrate deep into the bulk. This property, however, prevents them from unperturbed movement from the sample surface to the detecting unit of the experimental setup maintained under the regular pressure. The pressure gap can be overcome by, e.g. utilizing X-ray based *in situ* techniques supported by complementary *ex situ* measurements.

## This work

The main aim of the research reported in the present dissertation is to improve the understanding of the relation between the catalytic activity and the surface structure on the atomic length scale. For this purpose single crystal model catalysts were studied under ultra-high vacuum as well as under realistic conditions with the ambition to bridge the pressure gap between surface science and industrial catalysis. To this end, a new approach using high-energy surface X-ray diffraction with photon energies of around 100 keV combined with simultaneous mass spectrometry has been employed. In addition, conventional surface X-ray diffraction, X-ray photoelectron spectroscopy, Auger electron spectroscopy, low-energy

electron diffraction, scanning tunneling microscopy, temperature programmed desorption spectroscopy and reflection absorption infrared spectroscopy measurements were also performed.

The reported results can be divided into two parts. The first part is focused on structural studies of the surface of Pd-based model catalysts relevant for, e.g. CO and CH<sub>4</sub> oxidation. *In situ* high-energy surface X-ray diffraction studies of the surface structure of single crystals acting as catalysts in the process of CO oxidation under semirealistic conditions are reported for Pd(100) (**Papers I-IV**) and Pd(553) (**Paper V**). The second part of the results is focused on a multitechnique investigation of the structural and the adsorption properties of FeO<sub>x</sub> ultrathin films grown on Ag(100) and Ag(111) single crystals (**Papers VI-IX**).

The seemingly simple mechanism of CO oxidation is, in reality, not so clear when it comes to the surface structure of the catalyst. In the case of the Pd(100) surface, the active phase responsible for the reaction at high  $\frac{O_2}{CO}$  ratios, for example, has been under debate for a long time [8–10, and references therein]. The proposed candidates are namely a metallic surface with chemisorbed oxygen and a one-layer thick surface oxide. This discrepancy, on the one hand, largely depends on particular conditions while, on the other hand, the experimental results obtained by different techniques are not so easily comparable. The fast flow of the reaction and short surface residence time for the molecules introduces additional difficulties for experimental investigations [11, 12].

In the present work, the evolution of the surface structure of the catalytically active Pd(100) single crystal is described in detail for a broad range of CO and O<sub>2</sub> partial pressures. Structural models are proposed for different phases occurring on the surface. To establish the connection between the rate of CO<sub>2</sub> production and the state of the surface, simultaneous mass-spectrometry measurements, performed to follow the gas composition, are reported. The procedure of data acquisition and analysis is reported in detail as high-energy surface X-ray diffraction is a recently established technique, which required the development of the experimental approach as well as specialized software for data treatment.

Structural studies of vicinal surfaces of single crystal catalysts under reaction conditions are extremely important in order to take one step further towards the understanding of real catalysts and narrow down the material gap. Such surfaces expose atomic steps, which mimic the atoms on the edges of nanoparticles in real applied catalyst to a certain extent. Studies of vicinal surfaces are reported in the literature more seldom than for flat surfaces because the obtained results are more difficult to interpret.

In the present work, a Pd(553) single crystal, acting as a catalyst in the process of CO oxidation, was thoroughly studied. Similar measurements under similar conditions as for Pd(100) were done with the ambition to follow the evolution of the vicinal surface structure. The novelty of the work is that the structural changes were resolved for the first time under reaction conditions.

Thin films attract great attention because these two-dimensional materials exhibit specific structural and chemical properties that are not available in the bulk structures [e.g. 13, 14, and references therein]. In addition, because of the film-substrate interaction, the structural and the electronic properties of such systems are tunable allowing for a wide range of applications including heterogeneous catalysis [e.g. 15–17]. Iron oxides in particular were shown to be active in catalytic reactions of selective oxidation and dehydrogenation [e.g. 18, and references therein].

In the present work, we investigate the structures of  $\text{FeO}_x$  films grown on Ag(100) and Ag(111) substrates. Different phases, occurring on the surface under different preparation conditions and at different amounts of deposited material, are discussed and structural models are proposed. In addition, we study the NO adsorption properties of one layer thick FeO(111) films grown on both substrates. We compare the results of the present observations showing that this system readily adsorbs NO molecules at liquid nitrogen temperatures with results reported for NO adsorption on FeO(111)/Pt(111), where the NO adsorption is negligible under similar conditions [19].

The reported research work involved collaboration between scientific groups at Lund University (Sweden), the University of Florida (USA), DESY in Hamburg (Germany) and Chalmers Competence Centre for Catalysis in Gothenburg (Sweden).

My contribution to this project includes experimental work at synchrotron radiation sources DESY (Hamburg, Germany), MAX-lab (Lund, Sweden), ALS (San-Francisco, USA), ESRF (Grenoble, France), Diamond (Oxford, UK) as well as laboratory work at Lund University and the University of Florida, development of experimental equipment and relevant software for analysis of the obtained data as well as the actual analysis of the obtained results.



# Chapter 1

## Crystal Structure

In this chapter, the basics of crystallography are recollected. The atomic structure of single crystal surfaces is described. Surface reconstructions as a result of different preparation and experimental conditions are presented and discussed.

### 1.1 Crystal lattices

Different types of crystals can be found everywhere in nature and in practical applications. In fact the vast majority of materials are crystalline and, hence, the studies of crystal properties are of paramount importance for understanding, employment and improvement of their qualities. To be able to describe the structure of a crystal the basics of crystallography should be first introduced.

The main distinguishing feature of crystals is the periodicity of their structure i.e. the existence of a unit that can form an infinitely large array by repeating itself according to certain rules. This elementary building block is called a *motif* and together with the mechanism of repetition in space it completely defines a periodic structure. The simplest mechanism that exists in every periodic array is translation, which is defined by a set of non-collinear vectors establishing the directions of translation and the period of repetition. The smallest possible motif together with the corresponding basis is referred to as a *primitive unit cell*. Several primitive unit cells can be combined and treated as one larger non-primitive unit cell should it be convenient for a particular task. In Figure 1.1a, a primitive and a non-primitive unit cells are shown in red and blue colors respectively. It should be noted that, although they look different, two primitive unit cells represented by solid and broken red lines in the figure contain the same motif and repetition mechanism, which makes them identical in terms of periodic properties. By repeating the motif along the directions

defined by the unit cell basis with the period defined by the basis vectors magnitude, it is possible to produce an arbitrarily large array. In the case of a crystal structure, the motif is constituted by atoms and the three dimensional translational basis becomes the basis of the crystal lattice.

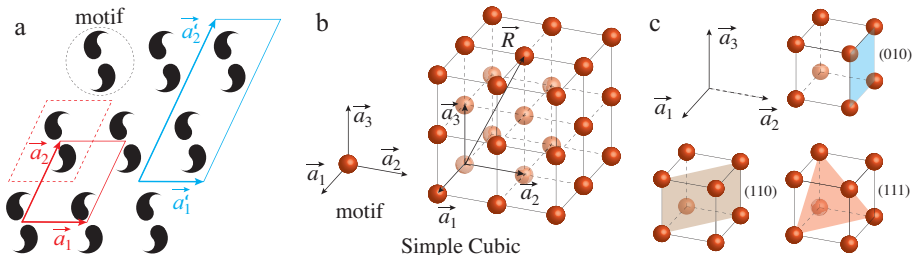


Figure 1.1: (a) A two dimensional periodic array with the motif consisting of two black symbols. Two examples of a primitive unit cell are shown with red solid and broken lines. One example of a non-primitive unit cell is shown with blue solid line. (b) A schematic view of simple cubic crystal structure with basis and motif. (c) Examples of low-index Miller planes in simple cubic unit cell.

In the case when the primitive unit cell of a crystal structure contains one atom as the motif and an orthogonal set of vectors  $\vec{a}_1$ ,  $\vec{a}_2$  and  $\vec{a}_3$  of the same length as the basis, it is called *simple cubic*. This structure is demonstrated in Figure 1.1b. The relative positions of any two atoms can be described by a vector  $\vec{R} = n_1 \cdot \vec{a}_1 + n_2 \cdot \vec{a}_2 + n_3 \cdot \vec{a}_3$  where  $n_1, n_2, n_3 \in \mathbb{Z}$ .

Although simple cubic crystal structure is the simplest possible periodic atomic arrangement, it is rarely found in nature due to the ease of distortion. In fact, the only known example of a simple cubic crystalline structure is the alpha form of polonium [20]. Two crystal structures with cubic symmetry, that are much more abundant in nature and are relevant to this work, are *body-centered cubic* and *face-centered cubic*. The motif of the primitive unit cell for these structures is constituted by two and four atoms correspondingly (see Figure 1.2).

Crystal lattices that may be constructed via discrete translations of a motif are conventionally called *Bravais lattices* after the French crystallographer Auguste Bravais who discovered that there are fourteen possible three-dimensional crystal lattices. Except three cubic symmetries discussed above, there is one triclinic, two monoclinic, four orthorhombic, two tetragonal, one rhombohedral and one hexagonal crystal structure [21, part 8].

When studying the periodic properties of a crystal structure, it is convenient to work with atomic planes rather than individual atoms. A set of three integer numbers  $h$ ,  $k$  and  $l$  called *Miller indices* is conventionally used to denote different families of parallel equidistant planes in a crystal lattice. These planes are often called *Miller planes* referring to their Miller indices. On the one hand, Miller indices can be described in terms of crystal lattice basis vectors. Namely, a plane intersects the basis vectors at  $\frac{1}{h} |\vec{a}_1|$ ,  $\frac{1}{k} |\vec{a}_2|$  and  $\frac{1}{l} |\vec{a}_3|$  of their

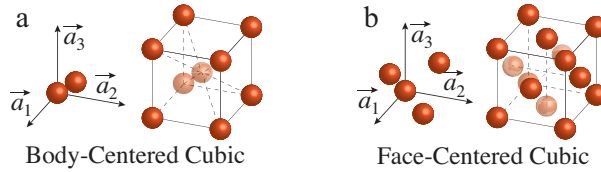


Figure 1.2: A schematic view of (a) body-centered cubic and (b) face-centered cubic crystal structures with basis and motif.

length (see Figure 1.1c for examples). On the other hand, they represent the coordinates of the vector perpendicular to the corresponding plane. The array of vectors representing all families of planes in a crystal constitutes a reciprocal lattice, which will be discussed in more detail in Chapter 4.

In the case when Miller indices are enclosed in round brackets,  $(hkl)$ , they denote the corresponding family of planes. In square brackets,  $[hkl]$ , they refer to the direction normal to the corresponding planes. Due to the symmetry, several families of planes can be completely equivalent, e.g.  $(100)$ ,  $(010)$  and  $(001)$  planes in cubic structures. Curly brackets,  $\{hkl\}$ , and triangular brackets,  $\langle hkl \rangle$ , are used in order to refer to all equivalent planes and directions respectively.

For more information and deeper insight into crystallography, the reader is referred to crystallography-related literature, e.g. Refs. [21, 22].

## 1.2 Crystalline materials

Although crystal lattices are perfectly periodic, crystalline materials often have a certain amount of disorder in the long range i.e. have a multi-domain structure. Due to impurities, defects, stress and strain acting against the uniform growth, most natural crystals cannot reach a significant size without breaking into *polycrystalline* form i.e. many small perfect crystals with the size from several nanometers and larger. Diamond, rock salt and quartz are examples of the possible growth of extended *single crystal* structure.

Polycrystalline materials are widely used for various applications. However, sometimes an extended perfect crystal lattice is required. This is important, for example, in optics or semiconductor electronics, when domain boundaries have a harmful impact on material properties. Another example relevant for this work, is model systems needed for thin film growth or studies in, e.g. heterogeneous catalysis. Since it is unnatural for most elements and compounds to grow in single crystal form, a great deal of effort is aimed at creating of such structures artificially. For that, materials are condensed from gas, liquid or amorphous state under specific conditions.

### 1.3 Crystal surfaces

In order to obtain a crystal surface, it is possible to cleave a bulk crystal. After polishing and cleaning, such a surface exposes a flat arrangement of atoms. In the case of a single crystal, the cleavage may be performed along one of the Miller planes. As a result it is possible to obtain an atomically flat surface with more or less known structure. Due to the extended area, such surfaces are often used as model systems to mimic more complex objects like for example facets of nanoparticles and to study their behavior in different physical and chemical processes related to, e.g. catalysis.

In a first approximation, it is possible to treat a surface as an unreconstructed termination of the bulk. The periodicity of the surface then is represented by a two-dimensional unit cell with the dimensions given in terms of the bulk unit cell. In Figure 1.3, the structures and the unit cells of  $\{100\}$ -,  $\{111\}$ -, and  $\{553\}$ -oriented surfaces of the FCC lattice are schematically demonstrated. These orientations of palladium and silver single crystal surfaces were studied in the current work.

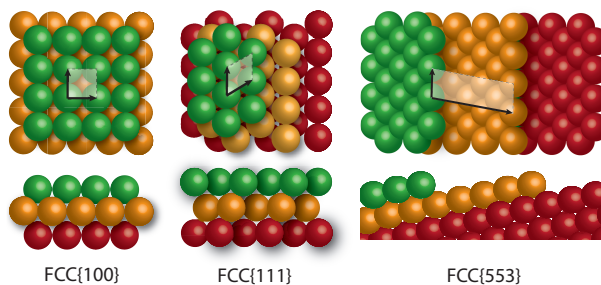


Figure 1.3: A schematic view of (a) FCC $\{100\}$ , (b) FCC $\{111\}$  and (c) FCC $\{553\}$  surfaces with primitive surface unit cells marked.

Because of the depletion of bonds, the formation of a surface leads to an increase of the total energy of the system. This happens because the *surface energy* addition is needed to create a surface. In order to reduce this effect, atoms within the top layers can rearrange themselves to a certain extent. In some cases, the structural changes are relatively mild while, when it is more energetically favorable, the surface may undergo a complete reconstruction. For example, the top-layer atoms of a silicon single crystal cleaved along the (100) plane tend to form atomic dimers instead of being evenly distributed (see Figure 1.4) [23–25].

If the surface layer has a different periodicity from the bulk, it is called a *superstructure*. Its periodicity then is conventionally given with respect to the unit cell vectors of the underlying substrate. Two types of notations are most commonly used, namely, the *Wood's notation* and the *matrix notation* [26]. For the silicon reconstruction described above, the complete Wood's description is Si(100)- $p(2\times 1)R0^\circ$ -2Si or shortly  $(2\times 1)$ . It includes from left to right the information about the substrate (a Si(100) crystal), the scaling of the su-

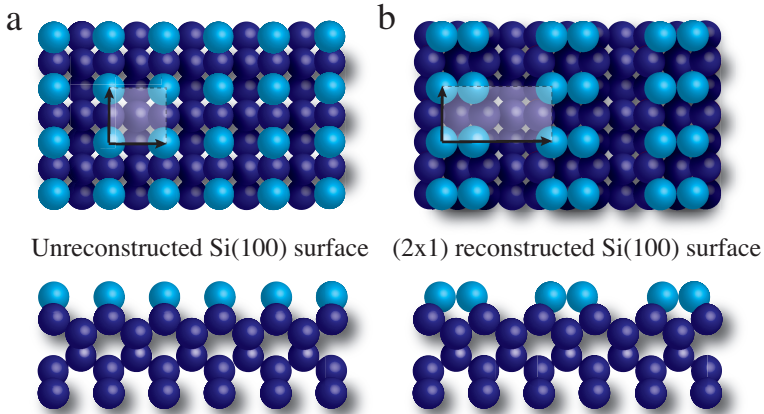


Figure 1.4: A schematic view of (a) an unreconstructed and (b) a  $(2 \times 1)$  reconstructed Si(100) surface.

perstructure unit-cell vectors with respect to the substrate unit cell vectors (one of the basis vectors of the superlattice unit cell is twice as large as the corresponding basis vector of the bulk unit cell while the other has the same length, symbol  $p$  indicates that the unit cell is primitive), the relative orientation of the surface unit cell with respect to the substrate (corresponding vectors are collinear) and the information about the superstructure (two Si atoms per unit cell). In the matrix form, the same structure can be described as

$$M_{Si(100)} = \begin{pmatrix} 2 & 0 \\ 0 & 1 \end{pmatrix}$$

showing the substrate and the orientation and the length of the superstructure unit cell vectors with respect to the substrate. These notations are also used when describing adsorbate layers. For more information about notation rules the reader is referred to Ref. [26].

A surface reconstruction can also occur in response to external conditions. A good example to illustrate surface reconstructions is the (110)-oriented surface of a tin oxide single crystal [27, and references therein], a surface which we have recently investigated. Although the  $\text{SnO}_2(110)$  surface is the most energetically stable non-polar termination of tin oxide [28], it nevertheless can adopt several structures depending on the preparation and experimental conditions. Namely,  $c(2 \times 2)$ ,  $(4 \times 1)$ ,  $(2 \times 1)$ , and  $(1 \times 2)$  reconstructions were reported over the years and are thoroughly reviewed in Ref. [27]. For example, as reported in Refs. [29, 30], annealing of a clean  $\text{SnO}_2(110)$  surface in oxygen at pressures higher than 1 Torr for several minutes at 700 K results in a  $(1 \times 1)$  “fully bridged” surface structure (see Figure 1.5a). Subsequent annealing of this system to 1000 K in UHV forces the bridging oxygen atoms to desorb leaving a bare  $(1 \times 1)$  stoichiometric surface (see Figure 1.5b). A longer annealing of this surface in UHV at temperatures higher than 1000 K, leads to formation of a “high-temperature”  $(1 \times 2)$  reconstruction (see Figure 1.5c).

Since it was observed for the first time in 1981 [31], the  $(4 \times 1)$  reconstruction of the (110)

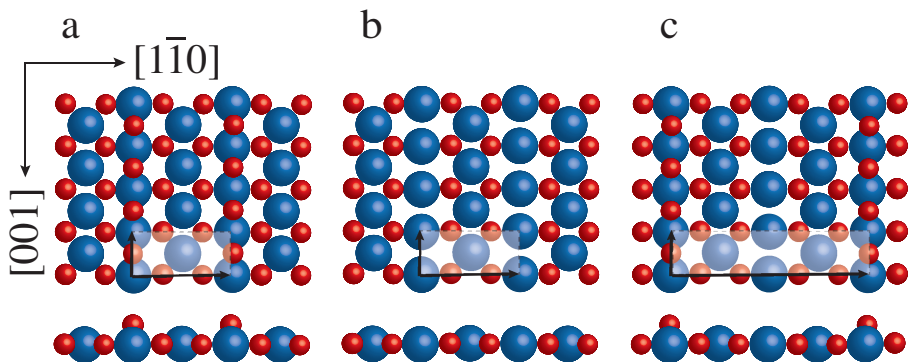


Figure 1.5: A schematic view of SnO<sub>2</sub>(110) (a) (1×1) “fully bridged” surface structure, (1×1) bare surface and (c) high-temperature (1×2) reconstruction. Oxygen and tin atoms are represented by smaller red spheres and larger blue spheres, respectively.

surface is the most frequently studied structure occurring on SnO<sub>2</sub>. It can be obtained by a long sputtering and annealing the surface at 1000 K under UHV conditions. The sputtering process removes O atoms more easily than Sn atoms increasing the Sn/O ratio in the surface region and leading to the following formation of a reconstruction. The exact structure of the (4×1) surface is, however, still under debate [e.g. 32–43]. Several models were proposed by different authors, namely, (4×1) arrangement of oxygen vacancies [30, 39, 41], add-rows of SnO [42] and SnO(101) overlayer producing (4×1) coincidence structure [35, 37]. Neither of these models was, however, confirmed so far. As tin oxide is considered for wide range of applications such as heterogeneous catalysis and gas sensing, the structure of its surface and therefore reconstructions occurring under different conditions are of a great importance and needs further investigations.

## Chapter 2

# Heterogeneous Catalysis

In this chapter the principles of heterogeneous catalysis are briefly discussed and the process of molecular interaction with the surface of a solid catalyst is shortly described.

### 2.1 Gas-surface interactions

Catalysis is a synthesis of science and technology, aimed to transform stable molecules with the help of special materials, catalysts. Heterogeneous catalysis in particular works with solid catalysts promoting reactions in solutions or gas environments [44]. In the present work the focus is on catalysts in reactions involving gaseous reactants.

One of the most important aspect of a heterogeneous catalytic reaction is the interaction of gas molecules with the surface of a solid catalyst, since the molecules in most cases can not penetrate deep into the bulk. This process includes initial adsorption, possible dissociation and diffusion, and desorption. On the one hand, if the molecules are bound too weakly they won't dissociate should it be necessary for the reaction. On the other hand, however, if the molecules are bound too strongly to the surface they won't be able to diffuse and desorb, which will result in poisoning and deactivation of a catalyst. Thus, the process of adsorption in a particular system should be thoroughly investigated in order to decide whether the chosen catalyst under specific conditions is efficient for a particular reaction.

If a molecule approaches a crystal surface it starts to interact with the atoms of the solid. This interaction can be either weak Van der Waals coupling with a relatively low energy involved (the process of *physisorption*) or a stronger chemical bond induced by a rearrangement of the valence electrons in both the gas molecule and the substrate (the process of *chemisorption*). In certain cases when the molecular bond is broken by the electron rearrangement the

chemisorbed molecules can dissociate on the surface [45].

The theory of adsorption was developed by the English mathematician and theoretical physicist John Edward Lennard-Jones in the beginning of 20-th century [46, 47]. In Figure 2.1 the simplified shape of potential curves for physisorption and chemisorption suggested by Lennard-Jones are schematically shown. When a molecule approaches the surface it first starts to feel a weak electrostatic polarization effect caused by the surface and an attractive Van der Waals force. At a certain distance the outer electronic orbitals of the molecule and the surface atoms begin to interact repulsively due to Pauli exclusion principle. The energetic minimum located between these two events is called physisorbed state and is rather shallow indicating the weak coupling of the molecule with the surface. The heat of adsorption (the energy that the desorption of the molecule requires) in the physisorbed state depends on the surface and the molecule and is usually on the order of  $10 \frac{kJ}{mol}$  [48]. If the molecule is not trapped in the physisorption minimum, it can approach closer to the surface and engage the valence electrons of the surface atoms into a chemical bond formation. Due to the rearrangement of the electronic orbitals the second energy minimum corresponding to the chemisorbed state is reached. This state is also called *associative chemisorption*, since the molecule preserves its identity. If then the molecule has enough energy to overcome the next activation barrier, it can dissociate and reach the energy minimum corresponding to a chemisorbed atom.

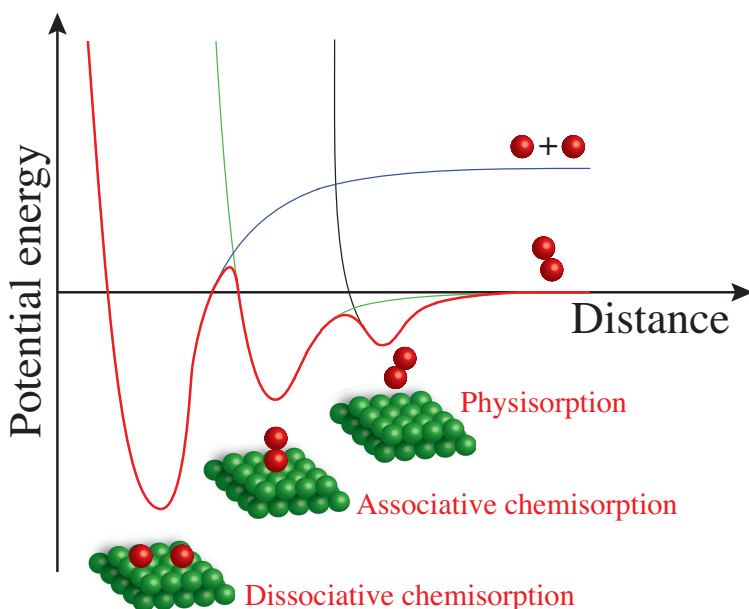


Figure 2.1: A schematic representation of the Lennard-Jones potential curve for a diatomic molecule approaching the surface of a solid.

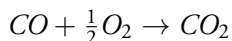
It should be mentioned that the picture discussed above is significantly simplified. Such factors like, e.g. the orientation of the molecule with respect to the surface and the local structure of the surface play an important role in determining activation barriers and, thus, in adsorption behavior. The height of the activation barriers depends also on the properties of the molecule and the catalyst. For example, molecular oxygen easily dissociates on most transition metals, whereas it hardly does so on Ag surfaces, where the activation barrier for dissociative adsorption is about  $15 \frac{\text{kJ}}{\text{mol}}$  [48].

## 2.2 CO oxidation

In the present work a considerable effort was devoted to studies of model catalysts surfaces in the catalytic oxidation of CO (**Papers I-V**).

Oxidation of CO is one of the best known and frequently studied reactions in heterogeneous catalysis because of two main reasons. Firstly, CO is a highly poisonous gas, which is produced in a vast quantity in the world as one of the products of fuel combustion processes in, e.g. car engines or power plants. It was therefore of great practical importance to find a way to reduce the harmful impact of exhaust gases on nature and human health. Secondly, the fact that CO oxidation reaction has only one product and proceeds over a wide range of pressures makes it an excellent probe reaction for studies of structural and adsorption properties of catalysts [4].

The interest for this reaction, which arose more than a hundred years ago [49, and references therein], is still significant. The process follows a seemingly simple scheme



which, however, requires the presence of a catalyst comprised of, e.g. Pd, Pt, Rh or their mixture at elevated temperatures [5, 6].

The catalytic reaction cycle begins with the diffusion of CO and O<sub>2</sub> molecules through the gas environment to the metal surface (see Figure 2.2) whereby they are adsorbed. Then, if the oxygen molecule receives enough energy from the surface to overcome the activation barrier, it dissociates into two oxygen atoms. The carbon monoxide does not dissociate due to much higher internal bond strength ( $1076 \frac{\text{kJ}}{\text{mol}}$  for CO vs.  $500 \frac{\text{kJ}}{\text{mol}}$  for O<sub>2</sub>) [48]. The next step is surface diffusion and the reaction of CO with O atoms. CO<sub>2</sub> molecules formed as the result of this process desorb from the surface (which costs about  $15\text{-}30 \frac{\text{kJ}}{\text{mol}}$  depending on the metal and the surface structure [44]) due to the exothermic nature of the reaction.

The reaction described above proceeds via the so called *Langmuir-Hinshelwood* mechanism. Two other mechanisms has also been identified, namely the *Eley-Rideal* and the *Mars-van*

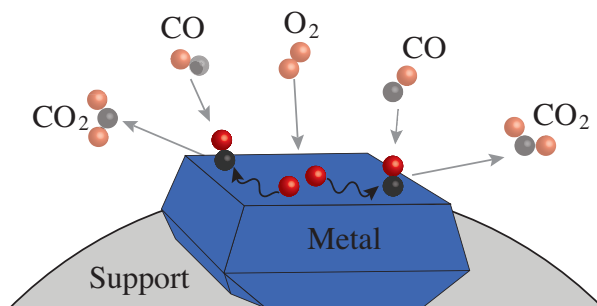


Figure 2.2: A schematic representation of CO oxidation over a solid catalyst. Two molecules of CO and one molecule of  $O_2$  adsorb on the surface and, after  $O_2$  dissociates, the species diffuse and recombine with the following desorption of  $CO_2$ .

### *Krevelen mechanisms.*

In the Eley-Rideal mechanism, one of the reacting species is accommodated on the surface and another reacts from the gas phase without being adsorbed [50]. The mechanism was proposed first for the atomic hydrogen gas reaction with hydrogen atoms on a hydrogen saturated tungsten surface [51] (see Figure 2.3a). This mechanism was also proposed for the CO oxidation reaction on a PdO(100)-O surface [52].

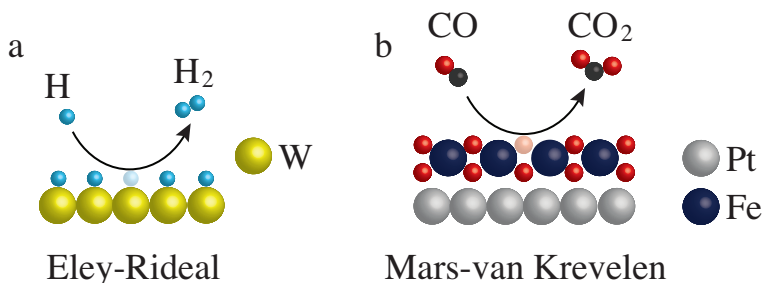


Figure 2.3: A schematic representation of the Eley-Rideal (left) and the Mars-van Krevelen (right) reaction mechanisms. The first is demonstrated by formation of  $H_2$  from atomic hydrogen gas dozed upon hydrogen saturated tungsten surface. The second is represented by CO oxidation over  $FeO_x$  grown on Pt(111).

In the Mars-van Krevelen mechanism, gas molecules react with and remove atoms inherently embedded in the surface of a catalyst. In the case of oxidation such a process is often observed in the presence of an oxide structure on the surface of a catalyst. The mechanism was suggested first for oxidation of aromatic hydrocarbons over a vanadium oxide catalyst [53]. The Mars-van Krevelen mechanism was also proposed in Refs. [54, 55] for the case of CO oxidation over  $FeO_x$  grown on Pt(111).

## Chapter 3

# Surface Oxides and Thin Oxide Films

In this chapter the formation of surface oxides and growth of thin oxide films on surfaces are presented and illustrated with examples.

### 3.1 Surface oxidation

In the current work the term *oxidation* applied to crystal structures will be used exclusively to refer to the formation of an oxide. The oxidation of a surface, thus, is a process when oxygen atoms interact with the outermost atoms of a crystal lattice, which results in the formation of a periodic oxide superstructure. Such *surface oxides* can appear in various situations when a certain amount of oxygen species is located in the vicinity of the surface. When the surface concentration of oxygen atoms reaches a critical value, in some cases it becomes energetically favorable for them to diffuse into the crystal lattice and form an oxide compound [56, 57]. This is common for metals as they are prone to forming oxides.

Depending on external conditions, different types of surface oxides can grow on a metal varying in stoichiometry, thickness, regularity etc. [e.g. 58]. In surface science experiments thin well-ordered surface oxides are conventionally grown by exposure of a clean metal in UHV to small amounts of a pure oxygen gas in conjunction with heating of the crystal which is often required [e.g. 59]. Similar structures can also occur on the surface of a heterogeneous catalyst under working conditions, e.g. in oxidation reactions [e.g. 60–62, and references therein].

In the current work a great deal of attention was paid to the (100) surface of a Pd single crystal acting as a model catalyst in CO oxidation reaction (see **Papers I-IV**). Based on the experimental results, it was shown that during the active phase of the reaction with

a small excess of oxygen a one-layer thick  $(\sqrt{5} \times \sqrt{5})R27^\circ$ -PdO(101) superstructure is present on the surface of the crystal. This surface oxide layer was found to be catalytically active towards CO oxidation previously under UHV as well as under reaction conditions [e.g. 4, 11, 60, 63, and references therein]. A schematic view of this structure is shown in Figure 3.1 along with the bulk unit cell of PdO. Under reaction conditions  $O_2$  molecules adsorb on the Pd surface heated to 600 K and dissociate in order to provide atomic oxygen species for oxidation of CO molecules. The presence of these oxygen atoms on the surface results in formation of surface oxide.

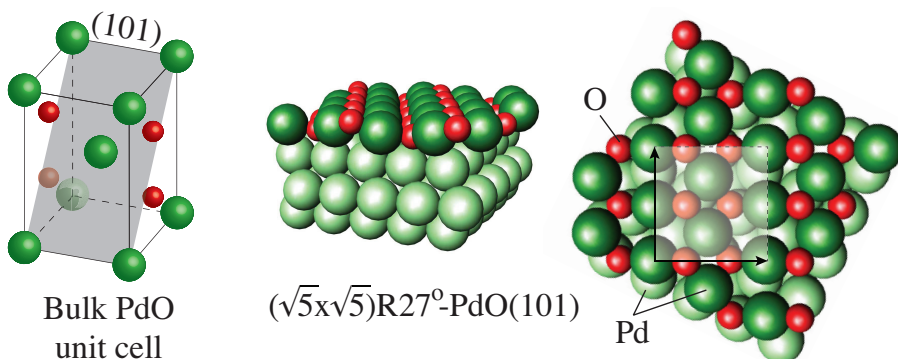


Figure 3.1: A schematic side and top views of Pd(100)- $(\sqrt{5} \times \sqrt{5})R27^\circ$ -PdO(101). The bulk unit cell of PdO is shown on the left.

It should be mentioned that the in-plane periodicity of a surface oxide may correspond to a certain crystallographic plane in the bulk form. In such a case the superstructure is described by the corresponding set of Miller indices, for example the  $(\sqrt{5} \times \sqrt{5})R27^\circ$ -PdO(101) superstructure. The periodicity of the oxide layer may, however, as well be different from any bulk oxide crystal plane. This happens firstly due to the fact that the surface is depleted of bonds and have different energy. Secondly, the interaction of the oxide layer with the substrate results in a distortion of the atomic lattice due to different unit cell dimensions. In such cases the stoichiometry of the oxide identifies the superstructure, e.g.  $Pd_xO_y$  overlayers growing on Pd(111) [64].

With a sufficiently high concentration of oxygen atoms in the vicinity of the substrate, surface oxides can grow thicker than one layer [e.g. 65]. Depending on the way the second and subsequent layers form, three growth modes, namely, the Frank-van-der Merwe, the Vollmer-Weber and the Stranski-Krastanov are distinguished (see Figure 3.2). In the Frank-van-der Merwe mode, every new layer starts to form when the previous is fully or almost fully completed. The Vollmer-Weber mode is characterized by the growth of separate islands, which tend to increase in height without wetting the surface. In the Stranski-Krastanov mode, the first layer fully or almost fully wets the surface and is followed by islands growth on top. In the case of Pd(100) model catalyst under CO oxidation con-

ditions with a high excess of oxygen, for example, the  $(\sqrt{5} \times \sqrt{5})R27^\circ$ -PdO(101) superstructure forms on the surface followed by the growth of thicker islands exhibiting the Stranski-Krastanov growth mode (**Paper IV**).

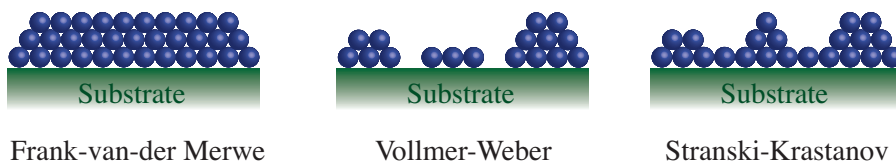


Figure 3.2: A schematic view of different superstructure growth modes.

### 3.2 Thin films

Uniform structures with the thickness from fractions of nanometer to micrometers forming on substrate surfaces are often called *thin films*. The exact definition is, however, missing. Most authors use this term when the film and the substrate are composed of different elements or compounds. Such films play an important role in many practical application ranging from semiconductor industry to heterogeneous catalysis. Iron oxide thin films grown on different substrates, for example, have shown a high performance as selective oxidation catalysts [e.g. 18, and references therein]. In the present dissertation, the studies of the structural and the adsorption properties of FeO films grown on Ag(100) and Ag(111) single crystal substrates are reported (**Papers V-IX**).

One of the usual ways to prepare a well ordered thin film under UHV conditions is deposition of material on a substrate. In the present work the FeO films were obtained by deposition of iron in the presence of oxygen (reactive physical vapor deposition (RPVD)) using an electron beam evaporator. This process is illustrated in Figure 3.3. Iron atoms evaporated from an iron rod by heating are directed at the surface of the crystal where together with oxygen they form a disordered FeO compound, which turns into an ordered film upon subsequent annealing.

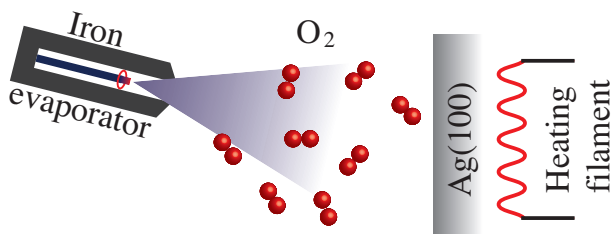


Figure 3.3: A schematic representation of a reactive physical vapor deposition process.



## Chapter 4

# Investigation of Surfaces

In this chapter, the experimental and the theoretical approaches that have been employed to perform the studies reported in the present dissertation are described. The principles of X-ray and electron diffraction are briefly explained with an emphasis on surface sensitive implementations. The basics of scanning tunneling microscopy as well as several spectroscopic techniques including XPS, AES, RAIRS, and TPD and their applications for studies of structural and adsorption properties of surfaces are discussed. The approach used to perform DFT calculations of surface structural properties is shortly summarized.

### 4.1 X-ray diffraction from single crystal surfaces

Like a periodic set of slits works as a diffraction grating in optics, a periodic atomic array acts similarly when exposed to electromagnetic radiation with a wavelength comparable to interatomic distances. It allows for employing the diffraction approach – recording the relative positions of the interference maxima of scattered radiation in order to calculate the periodic properties of an atomic structure.

The electromagnetic radiation wavelength is related to its energy via

$$\lambda_p(\text{\AA}) = \frac{h}{c \cdot E} = \frac{12400}{E(\text{eV})} \quad (4.1)$$

where  $h$  is the Planck constant,  $c$  is the speed of light in vacuum and  $E$  is the photon energy. X-rays in the energy range roughly from  $\sim 10$  keV to  $\sim 100$  keV, thus, have a wavelength on the order of  $1 \text{ \AA}$  or smaller and may be used as a probe for determination of a crystal structure in a diffraction experiment.

The first works discussing diffraction patterns arising from polycrystalline solids were published in the beginning of 20th century by Max von Laue and his co-workers [66] shortly followed by the results of William Henry and William Lawrence Bragg [67]. Since then X-rays were widely used for diffraction experiments with bulk samples. However, due to the complexity of experimental setup, only in the late 1970's an approach, employing X-rays impinging on a crystal surface under a grazing incident angle, was successfully applied for surface sensitive X-ray diffraction experiments [68].

#### 4.1.1 X-ray diffraction basics

##### Scattering of X-rays

In the energy region used in X-ray diffraction experiments, electromagnetic radiation has a negligibly small cross section with atomic nuclei and interact mainly with electrons within a solid body. Since electrons are charged particles, the oscillating electromagnetic field of the incoming wave sets them into forced vibrations. If no part of the incoming radiation energy is transferred to the electrons' kinetic energy (classical Thomson scattering [69]) the process is elastic and the vibrating electrons re-emit with the same wavelength. The electrons and hence the atoms containing them, thus, become secondary sources of electromagnetic radiation with the same properties as the initial incoming wave. This secondary radiation is referred to as elastically scattered and constitutes the dominant process in X-ray diffraction experiments.

A logical consequence of scattering of electromagnetic waves by electrons is the fact that the more electrons an atom has, the more secondary radiation sources can be created in the scattering process and hence the amplitude of the re-emitted radiation increases along with the increase of the atomic number (the intensity of the scattered radiation, according to basic wave mechanics, increases with the square of the atomic number). Practically this means that experimental techniques based on the photon scattering process (diffraction in particular) are more sensitive to heavier elements.

The phenomenon of diffraction of electromagnetic waves by a crystal lattice can be described as the process of interference of elastically scattered radiation. From wave mechanics it is known that, when two waves meet in the same point of space, they interfere with each other and form a wave with larger amplitude if they are in phase (constructive interference) and with smaller amplitude if they are out of phase (destructive interference). In the first approximation, it is possible to say that, when atoms in a solid emit secondary radiation, they can be considered as point-like sources of spherical waves, which propagate in space creating an interference pattern.

In Figure 4.1*a* the process of interference of two scattered electromagnetic waves is demon-

strated in two dimensions for two neighboring atoms. The distance between the black concentric rings represents the wavelength of the scattered radiation. It can be noticed that along the black arrows the secondary waves propagate in phase and, thus, interfere constructively. Depending on the path difference in terms of number of wavelengths, the zeroth, the first, the second, and so on orders of interference maxima are distinguished. Since the zero order direction coincides with the direction of the incoming beam, which blends with the interference signal, it is not trivial to use it for structural studies in diffraction experiments. In contrast, an X-ray detector positioned along one of non-zero order directions can directly record the intensity and the relative position of the corresponding interference maximum. This information can be directly used for structural analysis.

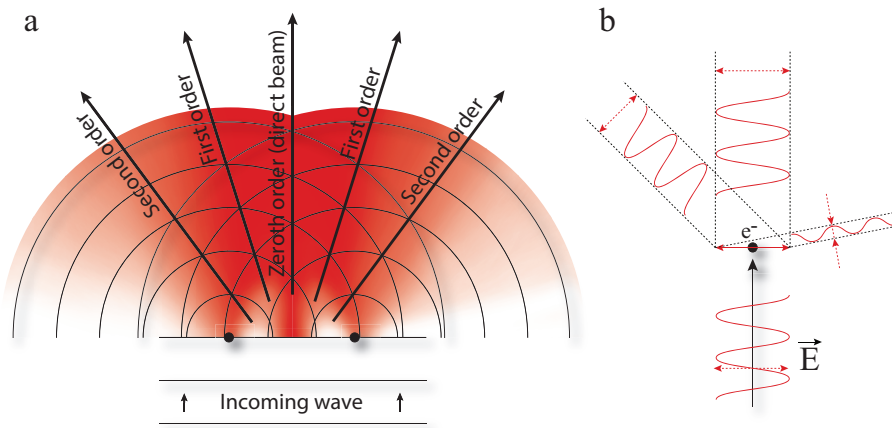


**Figure 4.1:** (a) Schematic 2D representation of interference process of two secondary waves with spherical wave fronts (the gradient of red color roughly represents the distribution of the radiation intensity of two scattered waves and the transmitted direct beam not accounting for the interference correction). (b) Schematic 2D representation of an electromagnetic wave scattering by a single electron.

The assumption that the fronts of scattered waves are spherical in reality, however, should be reconsidered. An electron is accelerated by the electric field of the incoming wave and oscillates in the same plane as the field vector. The amplitude and, hence, the intensity of the secondary radiation in this situation is the highest in the direction perpendicular to this plane and decreases with the angle of divergence as illustrated in Figure 4.1*b*. As a result, less intensity is scattered to high-order interference maxima making them weaker (demonstrated in Figure 4.1*a* by the gradient of red color).

It is worth mentioning that in diffraction experiments the scattered radiation is recorded at a certain distance from its origin, which is much larger than interatomic distances. The radius of the curvature of scattered wave fronts at such distances becomes large enough to consider the waves to be plane and their wave vectors to be collinear at every point of space. This is the Fraunhofer approximation – a conventional approach to evaluation of X-ray diffraction patterns.

## Determination of crystal structure by X-ray diffraction

A bulk crystal with a low concentration of defects can be treated, in practice, as an almost infinite three dimensional periodic array of atoms. In such an arrangement, parallel atomic planes exposed to electromagnetic radiation work as a diffraction grating creating an interference pattern due to cooperative scattering by coplanar atoms. For simplicity, this process can be viewed as “reflection” of the incoming radiation by parallel planes at certain incidence angles. The angular values where the “reflection” occurs depend on the interplanar distance within a set of parallel planes and the wavelength of the incoming radiation. This dependence was derived by father and son Braggs in 1913 and can be expressed as

$$n\lambda = 2d\sin\theta, n \in \mathbb{Z} \quad (4.2)$$

where  $\lambda$  is the wavelength of the incoming radiation,  $d$  is the interplanar distance and  $\theta$  is the incidence angle. In Figure 4.2a two waves scattered from adjacent planes are shown to be in phase when their path difference  $AC + CD$  is equal to  $n\lambda$ , thus, producing an interference maximum in the corresponding direction.

Different sets of planes have different interplanar distances and, therefore, when exposed to X-rays, produce secondary radiation interfering constructively in different directions at different incidence angles. In order to measure the signal coming from these sets of planes one needs to rotate the crystal, such that the corresponding reflection fulfills the Bragg condition (see Figure 4.2b). By recording the positions of the corresponding diffraction maxima with a photon detector for a given wavelength it is possible to obtain the interplanar distances for various sets of planes. In a real experiment this approach allows for determination of periodic structural properties and is widely used in, e.g. powder X-ray diffraction to determine the material composition, particle size and shape, partial concentration of components and several other parameters of polycrystalline solids.

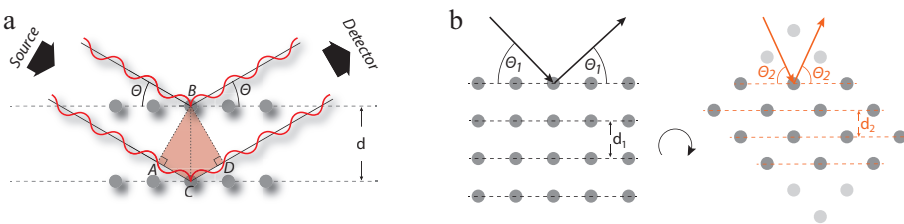


Figure 4.2: (a) Schematic 2D representation of diffraction of an incoming electromagnetic radiation by two parallel atomic planes. (b) Schematic 2D representation of difference in directions of constructive interference of the waves scattered by differently oriented atomic planes within a crystal

A more strict mathematical explanation of diffraction patterns produced by solid bodies can be done using the concept of momentum transfer of photons and is known as the von

Laue's formulation. In Figure 4.3a, two atoms, separated by a vector  $\vec{R}$ , are shown to be illuminated by electromagnetic radiation with a wavevector  $\vec{k}$ . After elastic scattering the length of the scattered wavevector  $\vec{k}'$  remains the same, while the direction of it can be different, since the secondary waves propagate in almost all directions. For elastic scattering the magnitude of  $\vec{k}$  and  $\vec{k}'$  is given by

$$k = |\vec{k}| = |\vec{k}'| = \frac{2\pi}{\lambda} \quad (4.3)$$

where  $\lambda$  is the wavelength of the incoming radiation. If treated like photons, X-rays can be characterized by their momentum

$$q = |\vec{q}| = |\vec{q}'| = \frac{h}{\lambda} = \frac{h}{2\pi} k \quad (4.4)$$

where  $h$  is the Planck constant. The vector of momentum is therefore proportional and collinear with the wavevector.

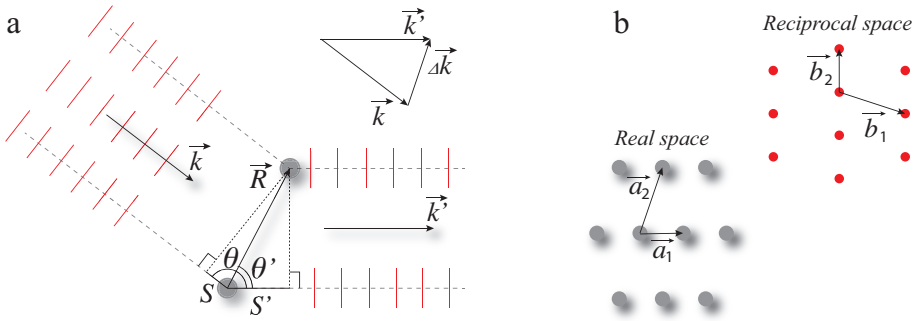


Figure 4.3: (a) Schematic 2D representation of elastic scattering of electromagnetic radiation by two atoms (Laue formulation). (b) Schematic 2D representation of a crystal lattice and the corresponding interference pattern (reciprocal lattice).

As before, two scattered waves interfere constructively along directions where they are in phase, i.e where their path difference ( $PD$ ) is equal to an integer number of wavelengths. Looking at the figure, it is possible to geometrically derive the dependence of this value on the mutual orientation of  $\vec{k}$  and  $\vec{k}'$ :

$$PD = S + S' = R \cos \theta' + R \cos \theta = \frac{\vec{R} \cdot \vec{k}'}{k} - \frac{\vec{R} \cdot \vec{k}}{k} = \frac{\vec{R} \cdot \Delta \vec{k}}{k} = n\lambda = n \frac{2\pi}{k} \quad (4.5)$$

From this

$$\vec{R} \cdot \Delta \vec{k} = 2\pi n, n \in \mathbb{Z} \quad (4.6)$$

or

$$\vec{R} \cdot \Delta \vec{q} = hn, n \in \mathbb{Z} \quad (4.7)$$

Conditions 4.6 and 4.7 are known as Laue conditions and show along which directions relative to vectors  $\vec{R}$  and  $\vec{k}$  (or  $\vec{q}$ ) two scattered waves interfere constructively.

In a three dimensional crystal lattice any two randomly chosen atoms can be involved into two scattering events separated by a vector  $\vec{R}$ . In this case the length and the direction of  $\vec{R}$  is defined by the lattice basis  $\vec{a}_1, \vec{a}_2, \vec{a}_3$  as  $\vec{R} = u\vec{a}_1 + v\vec{a}_2 + w\vec{a}_3$ , where  $u, v, w$  are integer numbers. Every pair of atoms within a crystal scatters X-rays and therefore produces an interference pattern according to conditions 4.6 or 4.7. It can be shown (see, e.g. [70]) that, due to the lattice symmetry, the interplay between constructive and destructive interference of the waves scattered by all atoms of a crystal results in a large number (infinite for an infinite crystal) of point-like diffraction maxima with well defined positions in space. These maxima are organized in fact in a new three dimensional periodic lattice with the basis  $\vec{b}_1, \vec{b}_2, \vec{b}_3$  such that every vector  $\vec{K} = h\vec{b}_1 + k\vec{b}_2 + l\vec{b}_3$  ( $h, k, l \in \mathbb{Z}$ ) fulfills the condition

$$e^{i\vec{K} \cdot \vec{R}} = 1 \quad (4.8)$$

for all lattice vectors  $\vec{R}$  of the corresponding crystal lattice. Basis vectors  $\vec{b}_1, \vec{b}_2, \vec{b}_3$  can be constructed from the crystal lattice basis as

$$\vec{b}_1 = 2\pi \frac{\vec{a}_2 \times \vec{a}_3}{\vec{a}_1 \cdot (\vec{a}_2 \times \vec{a}_3)}, \vec{b}_2 = 2\pi \frac{\vec{a}_3 \times \vec{a}_1}{\vec{a}_1 \cdot (\vec{a}_2 \times \vec{a}_3)}, \vec{b}_3 = 2\pi \frac{\vec{a}_1 \times \vec{a}_2}{\vec{a}_1 \cdot (\vec{a}_2 \times \vec{a}_3)} \quad (4.9)$$

or in a shorter way

$$\vec{b}_i \cdot \vec{a}_j = \begin{cases} 2\pi, & \text{if } i = j \\ 0, & \text{if } i \neq j \end{cases} \text{ where } i, j = 1, 2, 3 \quad (4.10)$$

From 4.10 it can be seen that each vector  $\vec{b}_i$  of the diffraction lattice is perpendicular to two vectors  $\vec{a}_j$  with different indices ( $i \neq j$ ) and have a length of

$$|\vec{b}_i| = \frac{2\pi}{|\vec{a}_i| \cdot \cos \phi} \quad (4.11)$$

where  $\phi$  is the angle between  $\vec{b}_i$  and  $\vec{a}_i$ . Due to the reciprocal dependence of the length of basis vectors, the arrangement of diffraction maxima is called reciprocal lattice. The relation between a real (crystal) lattice and the corresponding reciprocal lattice is schematically shown in Figure 4.3b.

In order to complement and summarize the concept of reciprocal lattice presented above, it should be pointed out that, in the process of X-rays scattering by a crystal, conditions 4.6 and 4.7 are fulfilled if and only if the change of the wavevector  $\vec{\Delta k}$  is a vector of the corresponding reciprocal lattice ( $\vec{\Delta k} = \vec{K}$ ).

The importance of the concept of reciprocal lattice is in the fact that in a diffraction experiment it is possible to measure the positions of interference maxima of the radiation scattered by a crystal i.e. positions of the nodes of the corresponding reciprocal lattice, and mathematically transform them in order to determine the real atomic positions.

### The Ewald sphere concept

A geometrical construct known as the Ewald sphere was introduced by the German physicist and crystallographer Paul Peter Ewald. It constitutes a convenient approach that helps to determine what part of the reciprocal lattice of a crystal is accessible to X-rays with a certain energy. The way it can be used is schematically illustrated in Figure 4.4.

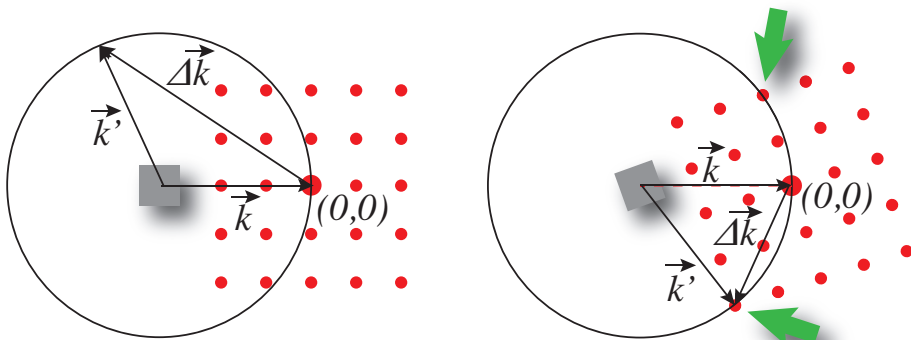


Figure 4.4: (a) Schematic 2D representation of the Ewald sphere intersecting the reciprocal lattice of a crystal at two different angles of azimuthal rotation.

With a photon detector it is possible to record any point of a reciprocal lattice, which can be reached by  $\Delta \vec{k}$ . In the case of elastic scattering, all such points are lying on the surface of a sphere with a radius equal to modulus of the wavevector of incoming radiation  $|\vec{k}|$  and the center lying at the origin of  $\vec{k}$ . The origin of the reciprocal lattice (the position of the direct transmitted beam) has a constant position at the end of  $\vec{k}$ . The whole diffraction pattern then rotates around this position with a rotation of the crystal under the incident beam sequentially intersecting the sphere with the areas where different diffraction maxima are located, making them detectable. This way - by rotating the sample - one can record a significant part of the reciprocal lattice with an X-ray detector. For the example in Figure 4.4 on the left panel, the Ewald sphere intersects the reciprocal lattice only in (00) position thus allowing for recording only this maximum. When the crystal is rotated, another diffraction spot marked with a green arrow becomes accessible for detection.

### 4.1.2 X-ray diffraction from surfaces

The electromagnetic radiation diffracted by an ideal infinite crystal forms an ordered array of infinitely narrow Bragg peaks. Their positions coincide with the nodes of the corresponding reciprocal lattice constructed as a Fourier transformation of a real atomic lattice. The Fourier transformation of a truncated crystal with a surface, as a two dimensional structure, creates a diffraction signal in the shape of infinitely thin rods - called *crystal truncation rods* - passing through Bragg peaks perpendicularly to the surface at every integer value  $\vec{k}_{\parallel}$ . In reality, the recorded signal also contains contribution from the subsurface and the bulk regions. Thus an interference pattern obtained in practice is a convolution of different diffraction signals. In Figure 4.5 the distribution of the scattered radiation is schematically shown with respect to the penetration depth of an incoming electromagnetic radiation. The diffracted signal from the bulk contributes mainly to Bragg peaks, while the subsurface and especially the surface region produce the signal that can be detected upon moving away from the maxima along the direction perpendicular to the surface.

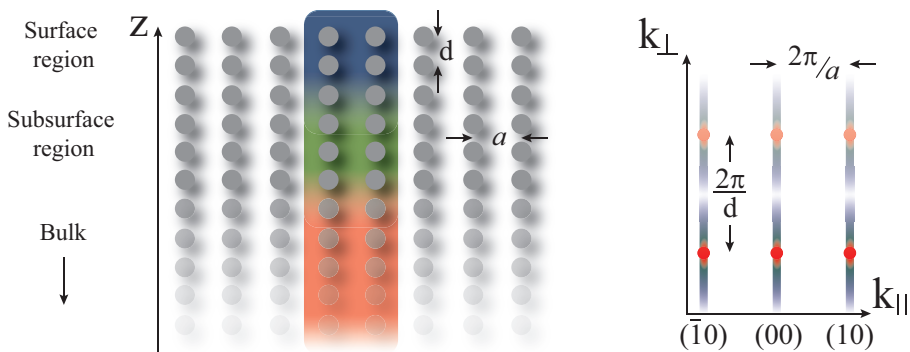


Figure 4.5: Schematic representation of a crystal exposed to electromagnetic radiation (left) and the corresponding diffraction pattern showing which part of the signal comes from different areas of the crystal (right).

The presence of a surface reconstruction or an adsorbate layer results in the appearance of additional diffraction rods in the pattern (see Figure 4.6). These rods are called *superstructure rods* and can be analyzed to determine the corresponding surface structure. For example, the surface reconstruction shown in panel *a* has a double in-plane periodicity as compared to the substrate while the adsorbate layer in panel *b* has a lattice constant 1.5 times larger than the size of substrate surface unit cell. In both cases the in-plane periodicity of the superstructure results in a denser in-plane distribution of the corresponding diffraction rods. Unless the thickness of the superstructure becomes significant, it is described by the surface step function that is rather narrow in the direction of the surface normal. This means that the intensity distribution along the superstructure diffraction rods does not have pronounced maxima and thus there are no Bragg spots lying on the SRs.

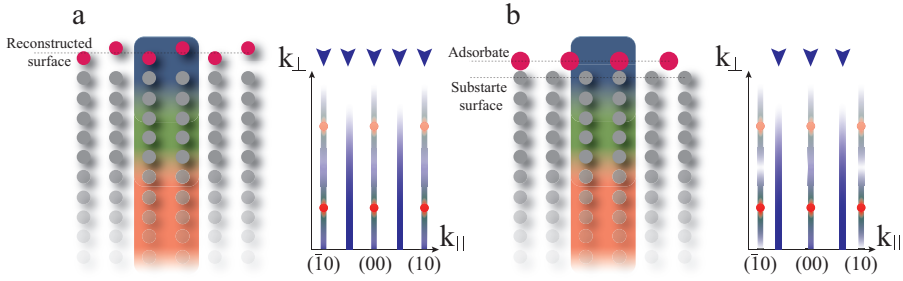


Figure 4.6: Schematic side-view representations of a crystal with a reconstructed surface (a) and an adsorbate layer (b) exposed to electromagnetic radiation and the corresponding diffraction patterns. The blue arrows show where the signal from the top layer contributes to diffraction patterns.

The step function (the profile) describing the structure of a surface dictates the shape of diffraction rods. Thus, analyzing the recorded signal - the intensity distribution along the CTRs and the SRs - and performing a reversed Fourier transformation, it is possible to determine the surface structure. In Figure 4.7 examples of experimentally measured CTRs and SR from a one layer thick FeO(111) film grown on a Ag(100) single crystal surface are shown. The details of this experiment and its results are discussed in **Paper VII**.

The intensity of the CTRs between diffraction maxima and the SRs over the whole length is extremely low in comparison to the Bragg peaks. This is due to the fact that scattered waves originating from the bulk interfere destructively and are completely canceled between the Bragg maxima and only atoms at the surface contribute to the signal. This contribution is small since the relative number of surface atoms is small. Thus, in order to record structural information about the surface using X-rays in reflection geometry it is necessary to confine the penetration depth by as few layers as possible. In surface X-ray diffraction it is achieved due to the grazing incidence.

### 4.1.3 Surface X-ray diffraction

In 1979, Marra, Eisenberger and Cho developed an experimental method employing X-rays ( $\text{Cu } K\alpha_{1,2}$ ,  $\lambda = 1.54\text{\AA}$ ) grazing incident on the surface of an epitaxially grown Al on a GaAs substrate [68, 71]. The authors used the fact that the refractive index of a solid body is less than unity for electromagnetic radiation in keV energy region. It results in occurrence of total external reflection at incident angles equal or less than a critical angle

$$\Theta_c = \sqrt{2\delta} \quad (4.12)$$

where  $\delta$  is the refractive index decrement, which is inversely proportional to the square of the photon energy (in the case of Marra *et al.*, for example, the critical angle for the GaAs crystal was  $0.286^\circ$ ). In conjunction with a diffraction phenomenon, a small penetration

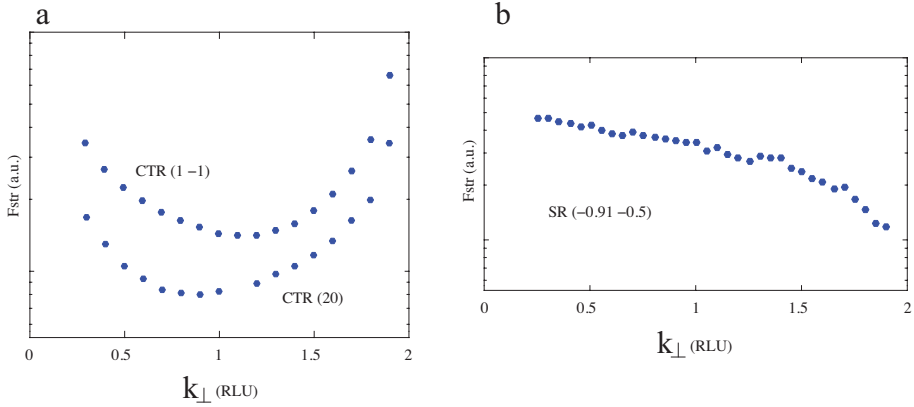


Figure 4.7: Experimentally measured CTRs (a) and SR (b) from a one layer thick FeO(111) film grown on a Ag(100) single crystal surface.

depth of grazing incident radiation allowed the authors to distinguish the diffraction signal from outermost atomic layers and study the atomic structure of the sample's surface. The method was called X-ray total-external-reflection-Bragg diffraction.

Experimentally the value of the critical angle can be precisely determined from reflectivity measurements. This is demonstrated in Figure 4.8 for a Pd crystal exposed to 85 keV X-rays, where the maximum of the reflectivity is achieved at  $0.08^\circ$  in terms of a double incident angle,  $2\Theta$ . Thus, for this system the value of the critical angle used in the current work is  $0.04^\circ$ . For a Ag crystal also studied in the current dissertation by means of the radiation of 18 keV energy the same angle is  $0.2^\circ$ .

After the pioneering works by Marra *et al.* more studies were done, e.g. [72, 73], and the methodology of the surface structure determination by grazing incident X-rays was optimized and turned into what we presently know as surface X-ray diffraction. A comprehensive description of X-ray diffraction from surfaces can be found in Refs. [74–76].

In surface X-ray diffraction experiments the scattered radiation is collected by an X-ray detector positioned behind the sample (see Figure 4.9). The recorded signal represents the intensity,  $I$ , of the diffracted radiation versus the wavevector change,  $\Delta \vec{k}$ . Depending on the type of the detector different approaches to data collection are utilized resulting in a different experimental geometry and a different data analysis procedures. Besides, the same amount of information can be recorded in a drastically different time period. For example, a point detector can probe only a small volume of reciprocal space at once and needs subsequent repositioning along a diffraction rod to record the intensity variation along its length. Since only the points of reciprocal space lying on the surface of the Ewald sphere are accessible for measurements, it means that, in order to move a point detector along a diffraction rod, it is necessary to constantly recalculate and change the relative position of the

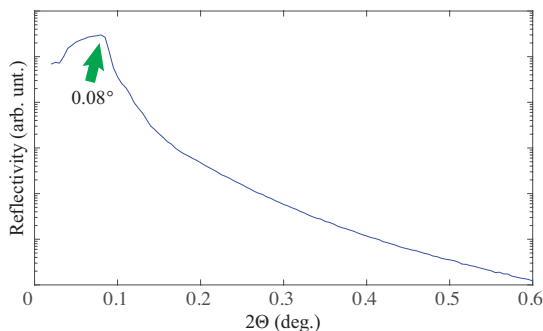


Figure 4.8: A reflectivity curve measured for a Pd crystal exposed to 85 keV X-rays.

sample surface, the incoming beam and the detector in accordance to a so called orientation matrix. Such a matrix is individual for every experiment and transforms the coordinates of a reciprocal lattice point, which should be measured, into the real coordinates of the point in space where the detector should be placed for that purpose. Additionally, the fact that diffraction rods are not infinitely thin results in the necessity to integrate the recorded intensity at every detector position while rocking the sample i.e. rotating it back and forth under the beam. The surface of the Ewald sphere in such a case crosses a diffraction rod at slightly different reciprocal coordinates moving through the thickness of a rod and the detector collects the full intensity of a rod's current segment. All this results in a long time required for determination of a surface structure and certain corrections arising due to the experimental geometry during the analysis [77].

Due to technological improvements, two dimensional X-ray detectors became available with time. Relatively small in area (for example  $83.8 \times 33.5 \text{ mm}^2$  Pilatus 100K installed at the I07 beamline at Diamond Light Source in England) they significantly facilitate the process of data acquisition due to the fact that a significant segment of a diffraction rod can be recorded in one rocking scan. The corrections of integrated intensity collected by such detectors are described in Refs. [78, 79]. These small area 2D detectors, however, still require repositioning during scanning of a rod.

Large area X-ray detectors (for example the PerkinElmer XRD 1622 AO & AP flat panel X-ray detector installed at the P07 beamline at the Petra III synchrotron in Germany), on the other hand, can record a large part of reciprocal space while the sample is being rotated on the diffractometer without any repositioning. They can be statically set behind the sample, which results in less mechanical movements. In combination with a high energy of the radiation, employment of such detectors facilitates the data acquisition even further. For example, at 85 keV energy of X-rays the PerkinElmer XRD 1622 AO & AP detector can record a  $10 \times 10 (\text{\AA}^{-1})^2$  slice of reciprocal space in one shot and a full set of structural data in about 15 minutes (see **Papers I, II** for the details) in contrast with days in the case of a point detector or hours in the case of a small area 2D detector. Besides that, the high

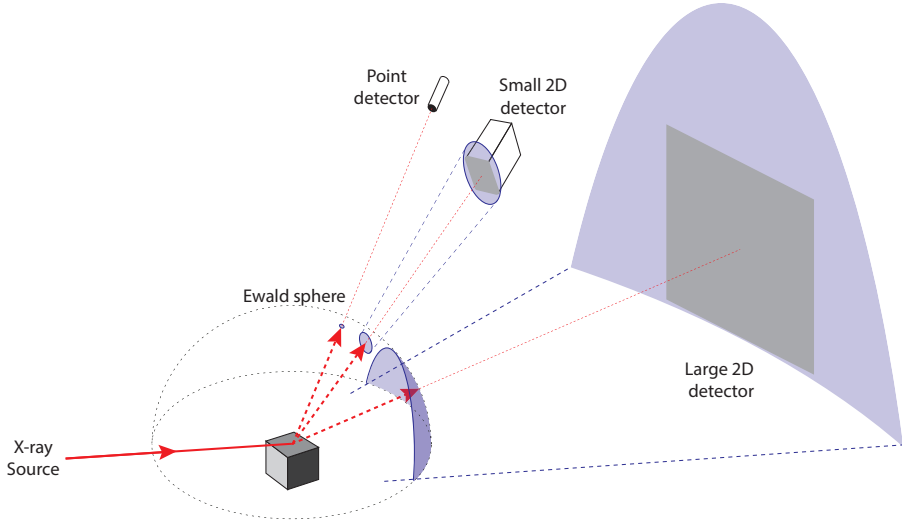


Figure 4.9: A schematic view of SXR D setup. Two types of detectors are shown to compare the part of reciprocal space that is recorded in one shot.

energy of the incoming radiation results in smaller scattering angles leading to a reduced amount of corrections required for data analysis (see **Paper II** for the details).

Regardless of how the SXR D data were obtained, the final result of an experiment is a set of diffraction rods, more particularly the values of structure factor,  $F_{str}$  ( $I \sim F_{str}^2$ ), versus change of the wavevector,  $\Delta \vec{k}$ .

$$F(hkl) = \sum_{i=1}^m f_m \cdot \exp^{2\pi i(a_m h + b_m k + c_m l)} \quad (4.13)$$

where  $f$  is the atomic scattering factor,  $a$ ,  $b$  and  $c$  are the coordinates of atoms in terms of the unit cell basis vectors,  $h$ ,  $k$  and  $l$  are the reciprocal coordinates, where the value of  $F_{str}$  is measured, in terms of the reciprocal unit cell basis vectors. The summation is done over all atoms belonging to the unit cell of a crystal lattice. The concept of atomic scattering factor is discussed in detail in Ref. [80].

Usually the basis of a reciprocal lattice is related to the surface, which produce diffraction rods, with  $h$  and  $k$  axes lying in the surface plane and  $l$  axis directed along the surface normal. In that case the wavevector change along the rods is represented by  $l$  coordinate and the shape of the rods is given in terms of  $F_{str}$  versus  $l$ . The shape can then be analyzed with the aim to determine the structure of the surface. For example, in Figure 4.10 some characteristic shapes of crystal truncation rods are simulated for the bare surface of a Ag(100) single crystal with different displacements,  $\Delta z$ , of the the top atomic layer along the surface normal. The shape of CTRs for a surface with the roughness  $\beta = 0.3$  is also shown in the

same figure (roughness is considered assuming the so-called  $\beta$ -model, in which surface level  $n$  has an occupancy  $\beta^n$  [81]).

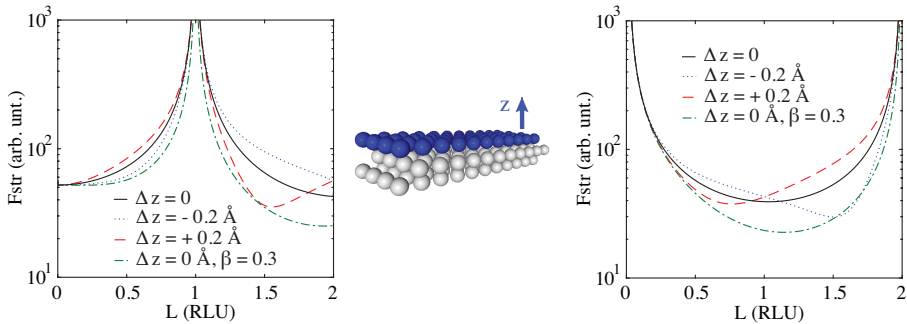


Figure 4.10: The shape of crystal truncation rods (01l) (left) and (02l) (right) produced by the bare surface of a Ag(100) single crystal. The top layer of silver atoms is differently displaced along the surface normal relatively to the zero level, which corresponds to the unperturbed bulk structure. The shape of CTRs for a surface with the roughness  $\beta = 0.3$  is also shown. The inset in the middle contains a ball model of the surface.

#### 4.1.4 Synchrotron radiation and beamlines

The surface X-ray diffraction experiments reported in the present dissertation were performed using synchrotron radiation. The high-energy diffraction data for Pd(100) and Pd(553) single crystals acting as catalysts in CO oxidation reaction (**Papers I-IV**) were recorded at the P07 beamline of Petra III at Deutsches Elektronen-Synchrotron (DESY) in Hamburg, Germany, while the data for one layer thick FeO(111) films grown on a Ag(100) single crystal (**Paper VII**) were collected at I07 beamline of Diamond Light Source in Oxford, England.

A very basic schematic representation of the operation principles of synchrotron sources is shown in Figure 4.11. An electron gun emits electrons that are accelerated and injected in a ring constituted by a number of straight sections maintained under UHV. At the end of every section a bending magnet is installed producing a magnetic field that forces the electrons to bend their trajectory and to follow the next straight section. In such a way, the electrons are “stored” in the ring keeping an overall round trajectory. A sequence of special cavities produces an electric field alternating with a radio frequency, which accelerate and decelerate electrons reaching a cavity at different moments in time. This eventually results in *bunching* of electrons that are moving inside of the ring with the cavity frequency. Every time a bunch of electrons enter an insertion device (undulator or wiggler) it starts to oscillate due to the frequent change of the polarity of magnets constituting the device. As the result of such oscillations electrons loose their energy at every turn and emit photons that are then directed into a beamline with an experimental station at the end, where they can be employed for, e.g. surface X-ray diffraction investigation. The energy losses are restored

upon every turn in the cavities. Due to a great number of electrons in every bunch the intensity of X-ray radiation produced by insertion devices is many orders of magnitude higher than that of, e.g. an X-ray tube. As a result, extremely weak surface signal can be recorded in a short time with a high signal to noise ratio. This was a significantly simplified overview of synchrotron operation, for more information the reader is referred to special literature, for example Ref. [69].

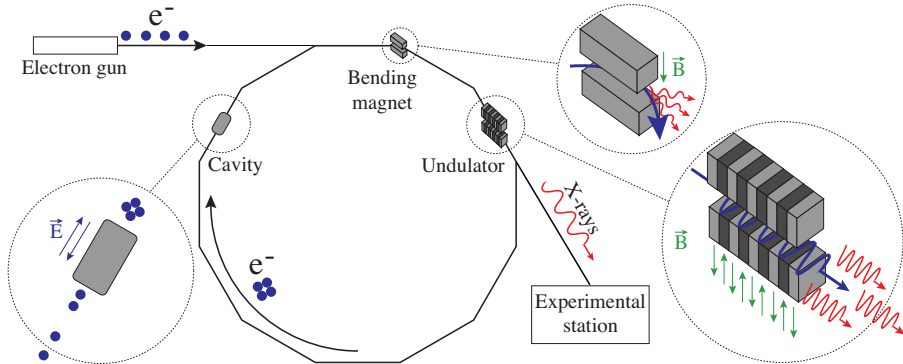


Figure 4.11: A schematic view of a synchrotron.

The P07 beamline of Petra III is designed for materials studies with hard X-ray radiation. A wide range of energies from about 30 to about 200 keV, is available for experiments. The size of the beam cross-section is also tunable between approximately  $3 \mu\text{m}$  and  $40 \mu\text{m}$ . The delivered flux is estimated to be on the order of  $5 \times 10^{10}$  photons/s [82]. A large two-dimensional  $410 \times 410 \text{ mm}^2$  Perkin-Elmer detector adapted for X-rays with the energy higher than 20 keV is available for recording of diffraction patterns (see Figure 4.12).

The I07 beamline at Diamond Light Source is a high-resolution X-ray diffraction beamline for investigating the structure of surfaces and interfaces under UHV as well as realistic conditions. The energy of the delivered X-rays can be tuned in the range between 6 and 30 keV. The beam can be focused to approximately  $100 \mu\text{m}$  and has the flux at the sample on the order of  $1 \times 10^{14}$  photons/s. The diffraction patterns are collected with a Pilatus 100K detector with the sensitive area of  $83.8 \times 33.5 \text{ mm}^2$ . The beamline endstation combines several experimental techniques, namely, SXRD, STM, XPS and LEED, with the possibility for sample transfer in UHV [83].

## 4.2 Low-energy electron diffraction

The fact that electrons can be treated as waves allows for considering them to be another possible probe for investigation of crystal periodicity. An electron's wavelength can be

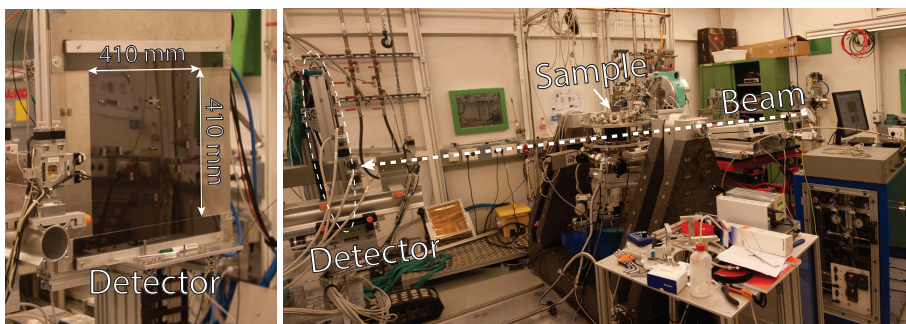


Figure 4.12: Photos of the experimental hutch at P07 beamline of Petra III, Hamburg, Germany and the two-dimensional detector used for recording of diffraction patterns.

calculated as

$$\lambda_e(\text{\AA}) = \frac{h}{\sqrt{2m_e \cdot E}} = \sqrt{\frac{150.4}{E(\text{eV})}} \quad (4.14)$$

where  $h$  is the Planck constant,  $m_e$  is the electron mass and  $E$  is the electron's kinetic energy. From here, electrons with energy from  $\sim 50$  eV and higher also have a wavelength on the order of interatomic distances.

In the late 1920-s, after theoretical work by Louis de Broglie devoted to wave-particle duality of electrons and experiments conducted by Clinton Davisson and Lester Germer [84] as well as early experiments by Harrison Farnsworth [85], the low-energy electron diffraction was established providing a possibility of probing the periodic structure of a crystal surface. Later, numerous experiments were performed to resolve the structure of reconstructed crystal surfaces, adsorbate layers, and thin films [e.g. 86–88, and references therein]. Nowadays, the LEED technique is utilized ubiquitously for both quick probing of in-plane periodicity and for an extensive structural analysis of ordered crystal surfaces.

Within the scope of the surface science approach, a few atomic layers are generally considered to be the surface of a solid body. From this perspective, low-energy electrons is almost a perfect probe, the sensitivity of which can be adjusted to the depth of a few Ångströms. Indeed, within the energy range between several tens and several hundreds of electronvolts, electrons interact strongly with matter and are quickly absorbed while traveling inside of a solid. This means that all observable effects of electron-solid interactions at these energies are confined by a number of outermost atomic layers and are not perturbed by the rest of the bulk.

The decay of an electron beam impinging on the surface of a solid body with an incident angle  $\theta$  (see Figure 4.13a) follows a reversed exponential first-order Beer law for the

absorbance of electromagnetic radiation

$$I(z) = I_0 \cdot \exp\left(\frac{-z}{\lambda(E) \cdot \cos \theta}\right) \quad (4.15)$$

which shows the number of electrons,  $I(z)$ , that remain not absorbed after the incident beam with the initial number of electrons,  $I_0$ , has reached a certain depth,  $z$ , into the solid. The critical parameter here is the *inelastic mean free path*,  $\lambda(E)$ . It essentially shows how far an electron beam of a certain energy can travel inside a certain solid material before it loses  $1 - \frac{1}{e}$  ( $\approx 0.632$ ) of its initial intensity due to inelastic scattering. It is clear from Equation 4.15 that electrons with a small IMFP are highly surface sensitive. The incident angle,  $\theta$ , also drastically changes the penetration depth since for incidence angles other than normal, the effective path of electrons in the solid increases reversely proportional to  $\cos \theta$ .

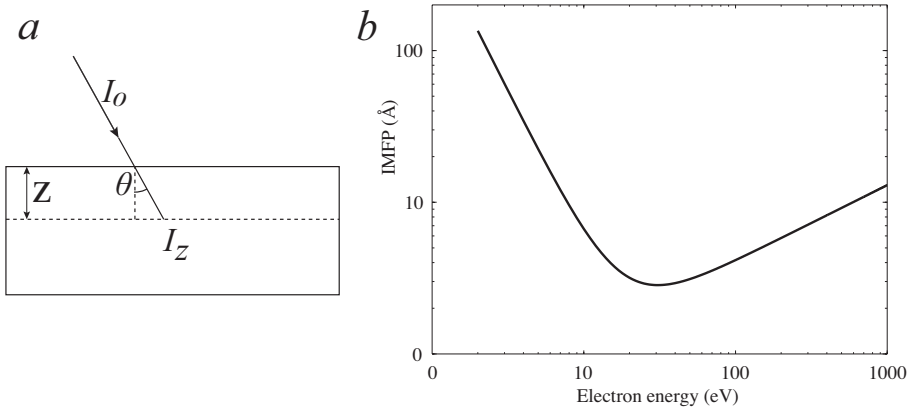


Figure 4.13: (a) Schematic representation of an electron beam penetrating in a solid body under an incident angle  $\theta$ . (b) The plot of empirically established dependence of electrons' IMFP on their energy for a hypothetical solid with a mean atomic diameter of 1 Å.

The empirical and approximate description of the inelastic mean free path of electrons in the energy range between 1 eV and 10 keV was given first by Seah and Dench [89]. The “universal curve” for a hypothetical solid with 1 Å mean atomic diameter proposed by the authors is shown in Fig. 4.13b. More experimental work was performed later [e.g. 90, 91] to increase the accuracy of the results proposed by Seah and Dench, however, the obtained corrections do not apply to the energy range used in the current study and thus are not discussed in this dissertation.

In Figure 4.13b, it can be seen that electrons with energy about 40-50 eV have the shortest IMFP and, thus, are most surface sensitive. Depending on the mean atomic radius of a particular material, the minimum of the IMFP curve slightly varies, however. In the case of one layer thick FeO(111) films grown on a Ag(100) and a Ag(111) single crystals, the best

experimental LEED patterns were recorded at the 40 eV electron energy (see Figures 4.14a and 4.14b correspondingly). Using Equation 4.15, it is possible to estimate the penetration depth of electrons into a silver crystal during the corresponding measurements. An incident electron beam normal to the surface will be attenuated down to 10% of its original intensity at the depth of about 12.9 Å, which is about 6-7 atomic layers of silver with a (100) stacking. This means that we could hardly probe any structure deeper than that. Besides, in this very rough estimation some aspects were not taken into account such as non-normal direction of the diffracted beams to the surface, intensity drop due to elastic scattering, influence of the surface roughness *etc.* decreasing the LEED probing depth.

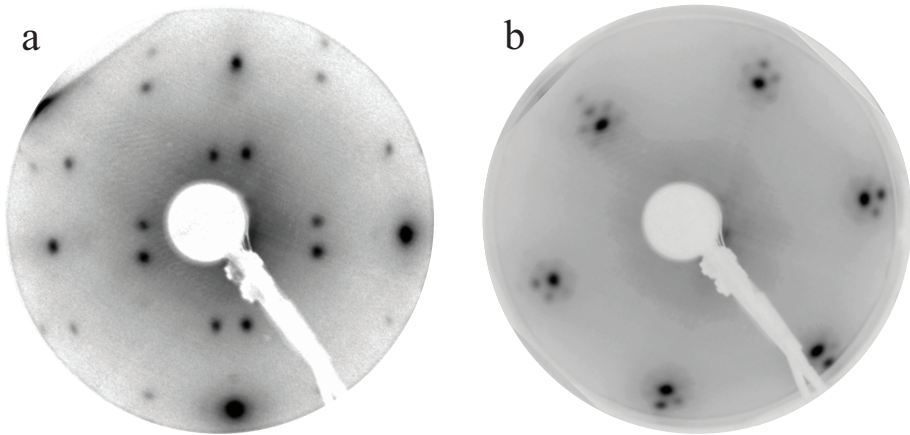


Figure 4.14: Experimental LEED patterns recorded at the 40 eV electron energy for one layer thick FeO(111) films grown on (a) a Ag(100) and (b) a Ag(111) single crystals.

A schematic view of a LEED setup is shown in Figure 4.15a. Mono energetic electrons produced by an electron gun impinge perpendicularly on the surface of a sample and are scattered backwards creating a diffraction pattern on a fluorescent screen. Since only elastic scattering contributes to the regular pattern, all inelastically scattered electrons should be prevented from reaching the screen in order to reduce the diffused background signal. This filtering is performed by an electric field created by a set of electrically conductive grids.

A schematic representation of the electron diffraction geometry process in reciprocal space is schematically shown in two dimensions in Figure 4.15b. The fluorescent screen in a LEED setup essentially shows a slice of reciprocal space corresponding to the surface of the Ewald sphere with a radius corresponding to the energy of an incoming radiation. In the pattern, therefore, one sees the cross sections of CTRs and SRs at the points where the sphere intersects them. By analyzing a LEED pattern it is, thus, possible to determine the in-plane periodicity of the surface. Besides that, by changing the energy of the incoming beam it is possible to record the out-of-plane variations of intensity along the diffraction rods. This approach is employed in quantitative LEED studies and gives a complete information

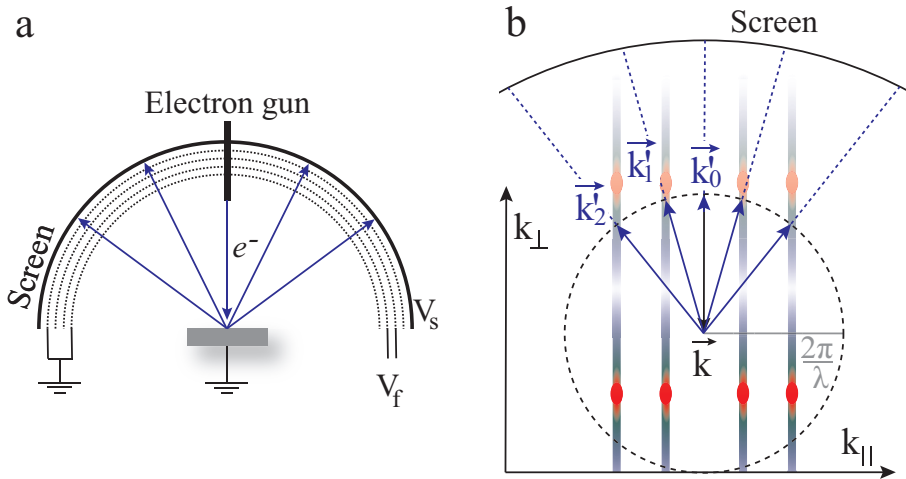


Figure 4.15: (a) Schematic representation of a LEED setup. (b) Schematic representation in reciprocal space of a scattering process in a LEED setup.

about the atomic scale structure of the surface. For a comprehensive description of LEED and pattern analysis techniques the reader is referred to, e.g. works of K. Heinz and M. Horn-von Hoegen's [87, 92].

Although LEED is an extremely versatile and useful experimental technique, it also has certain drawbacks. Namely, its application is confined by the requirement of low-pressure ambiance, due to a short mean-free path of electrons at atmospheric pressures, and difficulties in analysis of multiple scattering. These problems do not exist for X-rays, which weakly interact with matter and, thus, can be used in a high pressure ambiance. Besides, due to a small cross section, the scattering in the case of X-rays can be considered as a single-event elastic process.

It should be mentioned that, since diffraction is a collective phenomenon and strongly affected by structural disorder, in most cases it is difficult to observe non-periodic structures on the surface. Since non-periodic structures may be of great importance, one should be careful when correlating diffraction data with the sample structure in certain situations.

### 4.3 Scanning tunneling microscopy

Scanning tunneling microscopy was invented by Gerd Binnig and Heinrich Rohrer [93, 94]. It was a real breakthrough for surface science since it allowed for imaging of surfaces with atomic resolution. In this work, only a brief overview of the technique is given, while the reader can find more information in e.g Ref. [95]

The basic principle of STM is the vacuum tunneling of electrons between a solid and the end of a sharp tip probing a certain area of the surface in a raster mode. The tip, driven by piezoelectric motors, can approach the surface at a very short distance and, if the artificially created difference in potential is high enough, the electrons of either the tip or the solid can cross the vacuum barrier by quantum mechanical tunneling. The current between the tip and the surface caused by these electrons can then be detected and related to the distance between the end of the tip and the atoms of the solid. By moving the tip and recording a raster scan, it is possible to image the topography of the surface under study.

Figure 4.16 shows the electronic perspective of two solids (a tip and a sample), with different height of the Fermi level, that are brought close enough to each other to allow for electron tunneling. If the solids are electrically isolated from the ambience, a fast electronic transfer occurs aligning their Fermi levels and bringing the system to an equilibrium state. If instead one solid (the tip) is biased relatively to the other solid (the sample) by applying a voltage,  $V$ , it offsets the Fermi level of the tip by  $eV$ . This allows for a continuous flow of electrons, a tunneling current  $I_t$ , in one or another direction between the solids depending on whether  $V$  is positive or negative. This current depends exponentially on the separation between the electrodes, thus, providing a picometer resolution in measurements of the tip-sample distance.

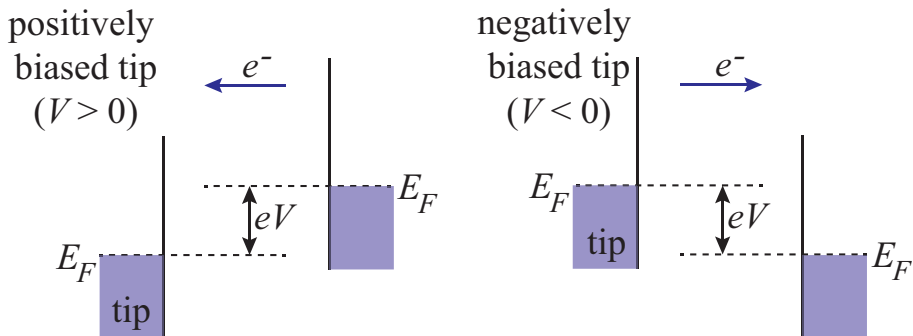


Figure 4.16: Schematic representation of the relative positions of the Fermi levels of the tip and the sample when the tip is positively biased (left) or negatively biased (right).

In STM experiments, an atomically sharp tip moves laterally in a close vicinity of the studied surface. The detected tunneling current is recorded and analyzed by a computer, which controls the expansion and contraction of piezoelectric elements driving the tip in three dimensions. There are two modes of operation, namely, constant height mode and constant current mode (see Figure 4.17). In the first case, the tip does not move in the vertical plane, while the change in the tunneling current provides the information about the topography of the sample. This approach allows for a faster scanning speed since the vertical mechanical movements of the tip are excluded. It requires, however, a low level of roughness of the surface and/or a small scan size because the tip can crash into any surface feature of a

nanometer size while failing to probe some pits on the surface due to the tunneling current interruptions at greater distances. In the constant current mode, as follows from the name, the tunneling current is retained constant by moving the tip closer to or further from the surface using a feedback controller while scanning. In this case, the topography of the sample surface is recorded using the positions of piezo-electric motors.

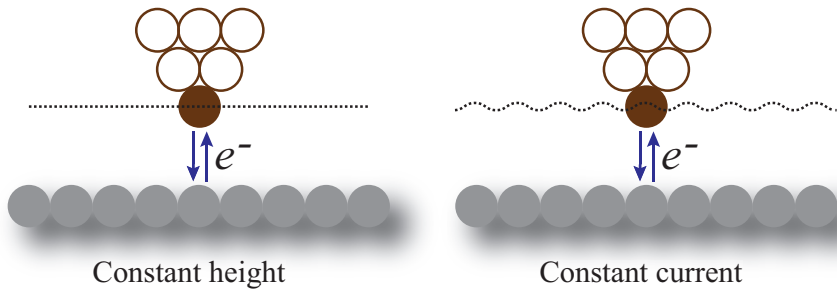


Figure 4.17: Schematic representation of the tip movement in constant current (left) and constant height (right) modes of operation of an STM setup.

Three examples of actual STM images are shown in Figure 4.18, with both successful results of the technique and difficulties in data analysis. In panels *a* and *b* two similar areas of the surface are shown. The studied structure is one layer thick FeO(111) film grown on a Ag(111) single crystal. The size of the recorded area is about six by six nanometers and the small round protrusions supposedly correspond to the surface atoms. However, one should always be aware that an STM setup records not the physical but the electronic structure of the surface, although in some cases the last one closely enough represents the first one. Depending on the electronic state of the atoms of a surface the electron tunneling can be more or less feasible resulting in a difference in the apparent height in an STM image. In the images, the color scale represents the apparent height of the atoms ranging from -29 to +14 pm in panel *a* and from -22 to +58 pm in panel *b* for the darkest and the brightest areas correspondingly. This height difference shows the variation of the electronic structure of the surface, which also indirectly includes the structural contribution. The FeO(111) film has a hexagonal long-range periodicity, which can be represented by the (9×9) surface unit cell resulting in the apparent periodic variation of the surface height in the STM images. Additionally, it can be noticed that two images have different overall appearance although they represent the same structure. This is due to the fact that the electronic structure of the tip also affects the recorded topography of the surface. During the scanning process the tip is prone to changes due to contact with the surface atoms or molecules that may be present on the surface or in the ambiance. By picking up or losing material from the end, the tip alters the tunneling current and, thus, the apparent surface structure.

In Figure 4.18*c* the STM image of FeO islands on a Ag(111) substrate is shown. The specific appearance of the islands tells an experienced user that the picture is not real but produced

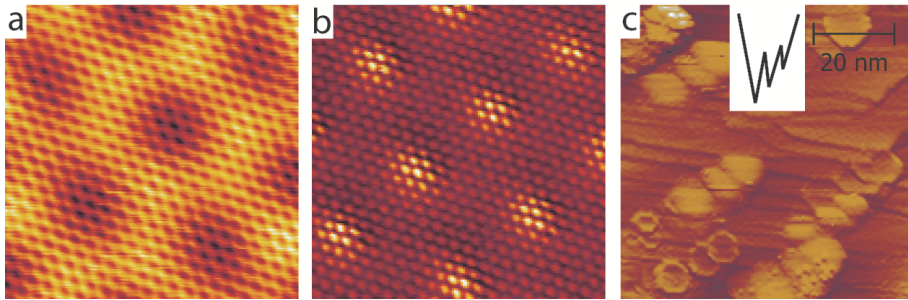


Figure 4.18: STM images of a one layer thick FeO(111) film grown on a Ag(111) single crystal. (*a – b*) Similar areas of the surface imaged with atomic resolution in two different states of the tip. (*c*) The image with artifacts caused by the tip asymmetry (a possible shape of the tip is shown in the inset).

due to the tip asymmetry. A possible shape of the tip producing such a signal is schematically shown in the picture inset. When scanning over the flat terrace, the vertical position of the tip is not affected by the presence of additional tip ends, but as soon as it approaches a step edge or an island, three different parts of the tip produce three independent pictures of the feature that are superimposed in the resulting image.

To draw a conclusion in this section, it is possible to say that STM experiments provide great possibilities to study surface structure directly with atomic resolution. However, the analysis of acquired data requires patience, accuracy and a lot of experience, since the apparent surface topography is significantly affected by the electronic structure. Additionally, STM images should be treated as a convolution of the surface electronic configuration and the shape of the tip, which can create artifacts that are not real. Moreover, the tip shape is not always constant but can change over the time resulting in different appearance of the surface structure. It is also important to mention that, due to the absence of electrons that can tunnel in insulators, STM experiments are limited to electrically conductive samples. In the case of non-conductive samples, one might want to use other experimental techniques like atomic force microscopy (AFM), working in a similar way as STM, but with the basic principle based on the attractive force between the sample and the tip.

## 4.4 Spectroscopy

Spectroscopy is a general name for a number of experimental techniques aimed at recording *spectra*. Historically, the word “spectrum” is associated with visible light and its dispersion by a prism. Later it was extended to all kinds of electromagnetic radiation and refers to the intensity of radiation as a function of its energy.

#### 4.4.1 X-ray photoelectron spectroscopy

Due to a high surface sensitivity and the broad chemical information that is provided, XPS has become a widely used experimental technique in surface science. It allows for determination of the chemical composition and the oxidation state of the elements in the surface region, which yields information about the structure of the sample surface and the presence of adsorbates.

The experimental approach is based on the photoelectric effect explained by Einstein in 1905 [96]. The incoming photons of energy  $h\nu_0$  can be absorbed by atoms of a solid and excite their core electrons. If the photon energy is high enough to transfer electrons beyond the vacuum level, they can be ejected from the surface with kinetic energy  $E_k$  (see Figure 4.19)

$$E_k = h\nu_0 - (E_b + \phi_s) \quad (4.16)$$

In Equation 4.16,  $h$  is the Planck constant,  $\nu_0$  is the frequency of the incoming electromagnetic radiation,  $E_b$  is the binding energy of the ejected electron respectively to the Fermi level of the sample and  $\phi_s$  is the sample's work function i.e. the energy required to remove an electron from a solid.

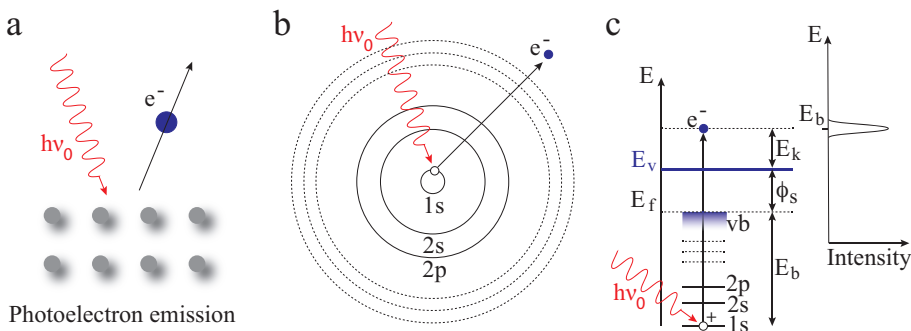


**Figure 4.19:** Schematic representation of (a) a photon's interaction with matter resulting in a photoelectron emission; (b) an atom with electronic orbitals (due to absorption of an incoming photon, an electron in the  $1s$  orbital is excited and escapes the atom leaving a positively charged hole behind); (c) energy levels of a similar atom and the corresponding  $1s$  photoelectrons' kinetic energy distribution recorded by a detector after exposure of the sample to  $h\nu_0$  X-rays.

The emitted electrons are called *photoelectrons* and are collected by an XPS spectrometer, e.g. [97, 98], which records their kinetic energy. The binding energy can then be easily calculated using Equation 4.16 and presented as a spectrum showing the distribution of the detected electrons. In many cases it is possible to determine the chemical composition

of the sample directly from the spectrum by comparing the values of binding energy where the intensity peaks are detected with the references for different chemical elements [99].

The higher the nuclear charge of an atom the higher the binding energy of a given core level (e.g. the binding energy of  $O 1s_{\frac{1}{2}}$  electrons is 532 eV while it is 7114 eV for  $Fe 1s_{\frac{1}{2}}$ ) and also the higher the principal quantum number of the electronic shell the lower is the binding energy (e.g.  $Fe 2p_{\frac{1}{2}}$  electrons have the binding energy of 723 eV only) [100]. The full list of binding energy values can be found, e.g. in the Handbook of X-ray Photoelectron Spectroscopy [99] or in the X-ray Data Booklet [101].

Due to a short mean free path of photoelectrons XPS measurements are highly surface sensitive. However, it introduces also one of the drawbacks of the technique when it comes to *in situ* studies, namely, the requirement of low pressure in the experimental chamber. Conventional XPS setups work under high or ultra-high vacuum conditions where the pressure is lower than  $10^{-6}$  mBar. Modern ambient pressure XPS setups can, due to a system of differential pumping and electronic lenses, operate under significantly higher pressures (up to about 1 – 10 mBar or even higher), which is enough in many cases to cover the pressure gap between model experiments and real operation in, e.g. heterogeneous catalysis. In spite of the pressure limitation, XPS measurements can provide valuable information about the sample, for example in studies of thin film growth, adsorbate layers *etc.*

The chemical surrounding affects the oxidation state of atoms in a solid and hence the energy of their core electrons due to a change in Coulombic attraction to the nucleus. It results in almost all cases in a shift of spectral peaks to higher or lower binding energy depending on the oxidation state of atoms. The higher the formal oxidation state an atom has the higher the value of the binding energy of its core electrons is in comparison with a lower oxidation state of the same atom. The spectral shifts are called chemical and can be analyzed with the aim to determine the surface composition and the presence of adsorbate structures [102]. Examples of XPS spectra analysis can be found in any XPS related literature, e.g. in Ref. [103].

A difficulty in XPS data analysis, which often arises, is too low energy resolution. Small changes in the oxidation state of atoms may result in appearance of two peaks subtly shifted with respect to each other. If this shift is on the order of tenths of electron volt, it may be non distinguishable for lab sources [100]. Using third-generation synchrotron sources, however, the energy resolution increases to about 50 meV or better [69]. Besides the energy resolution, the element sensitivity of the technique is much greater while using synchrotron radiation. The chemical composition can be determined down to a fraction of a per cent due to enhanced brilliance of the light.

Another advantage of synchrotron based XPS is a possibility to focus the beam down to micrometers and even in some cases to tenths of nanometers in order to acquire spatially

resolved information about the surface of the sample. Besides, by adjusting the monochromator at a synchrotron's beamline, it is possible to change the energy of the incoming photons. It allows for probing of the sample at different depths. In this case, one however should be aware of the possibility to hit the absorption edge of one of the studied materials.

#### 4.4.2 Auger electron spectroscopy

The process of electron emission induced by incoming radiation can consist not only of photoelectrons escaping the sample surface as discussed in the previous section but also in autoionization process within an excited atom. It is demonstrated in Figure 4.20. The electronic vacancy on a core level, which has appeared due to emission of an electron excited by incoming X-rays or electron beam, can recombine with another electron from an electronic shell of a lower binding energy. The energy released in this process is equal to the difference in binding energies between two electronic shells involved. As this energy has to be utilized, one of the following processes can occur: a photon can be emitted carrying away the released energy giving rise to X-ray fluorescence, or a third electron (Auger electron) can be excited escaping the solid. The second process is dominant for shallow core holes and light elements ( $Z < 15$  for holes on K electronic level), but not for elements with  $Z < 3$  (H and He), because they simply don't have enough electrons. For holes on L and M electronic levels Auger emission can be detected for the element with  $Z$  up to 50 [104].

The kinetic energy of an Auger electron can be measured in Auger electron spectroscopy providing information about the atomic core levels in the studied solid via

$$E_{kin} = E_{1s} - E_{2s} - E_{2p} - \phi \quad (4.17)$$

where  $E_{kin}$  is the measured kinetic energy of the Auger electron,  $E_{1s}, E_{2s}, E_{2p}$  are the values of binding energy of corresponding electronic shells and  $\phi$  is the sample's work function. The levels discussed here,  $1s, 2s, 2p$ , are just an example, while in the real measurements various electronic transitions can be detected. From 4.17 it can be seen that the kinetic energy of Auger electron does not depend on the energy of incoming photons causing the appearance of initial core hole.

As in most AES setups electron beam is used to induce the excitation process, many incoming electrons undergo multiple energy losses and are backscattered to the detector (secondary electrons). It results in a large background in the spectra, which makes it difficult to identify the peaks caused by Auger electron emission. This difficulty can be overcome by differentiating the distribution of the kinetic energy of electrons,  $N(E)$ , and plotting  $\frac{dN(E)}{dE}$  against  $dE$ . In this way, small Auger contributions to the spectra are more easily detectable. An example is shown in Figure 4.21, where the spectra obtained for the clean surface of a Ag(111) crystal (on the left) and for 1.5 ML FeO(111) grown on Ag(111) (on the right) are

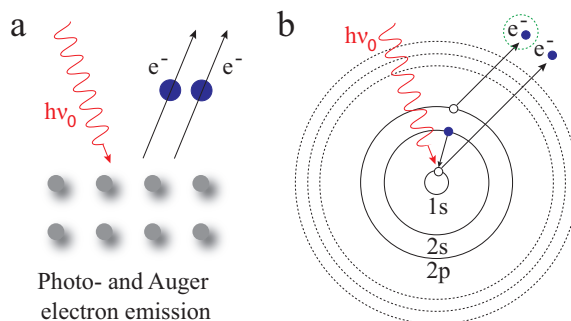


Figure 4.20: Schematic representation of (a) a photon's interaction with matter resulting in a photo- and an Auger electron emission; (b) an atom with electronic orbitals absorbs an incoming photon, an electron in a 1s orbital is excited and escapes the atom leaving a positively charged hole, which recombines with a weaker bound electron from another electronic shell releasing energy for yet another electron (marked with green dashed circle) to escape the solid).

presented in derivative mode. For small coverages of about one monolayer, the ratio of corresponding FeO peaks can be used to determine the amount of material deposited on the surface of a crystal, given that there is a reference measurement of a known coverage.

Since AES works with electrons, this experimental technique is also limited to low pressures.

#### 4.4.3 Reflection absorption infrared spectroscopy

In order to obtain understanding of chemical processes on the surface of a solid catalyst, the information about adsorbed species on atomic level is required. Employment of reflection absorption infrared spectroscopy allows for identification of the adsorbed species and their chemical interaction with the catalyst, and was originally demonstrated for supported catalysts by Eischens *et al.* [105]. Moreover, sometimes it is possible to determine the molecular adsorption geometry and occupied surface sites as well as interactions within the adsorbate layer, especially if a model catalyst and a probe molecule, e.g. CO or NO, are studied [44].

Due to the interaction of the electric field of the incident radiation with the molecular dipole moment, vibrational and rotational excitation of molecules can occur when they are exposed to infrared light of a certain frequency [106]. By recording the spectrum of IR light absorption in a certain interval of frequencies it is possible to determine the discrete levels of rotational and vibrational energies of a probe molecule [107]. Comparing these values with the value for the same molecule in the gas phase, it is possible to analyze the interactions of the molecule with its surrounding. For example, the value of the N-O stretch frequency in the gas phase is  $1860\text{ cm}^{-1}$ . Adsorbed on FeO(111) single layer grown on a Ag(100) single crystal (one of the model systems studied in the current work) at 90 K, however, NO molecules exhibit a lower stretch frequency of  $1821\text{ cm}^{-1}$  at a relatively

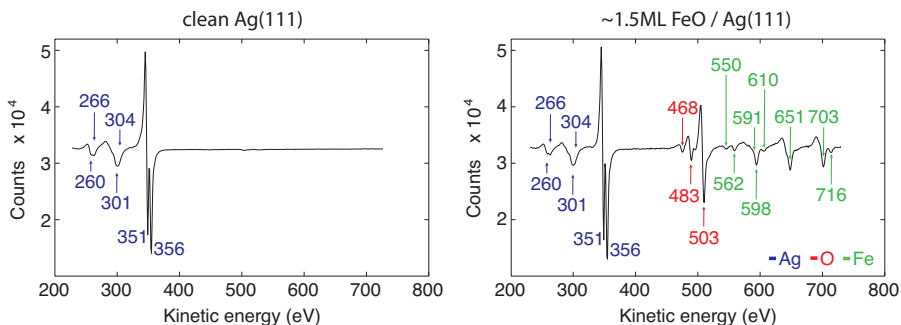


Figure 4.21: The Auger spectra obtained for the clean surface of a Ag(111) crystal (on the left) and for 1.5 ML FeO(111) grown on Ag(111) (on the right). The values of kinetic energy corresponding to the peaks are given color coded.

low coverage (the sample was exposed to about 0.1 Langmuir of NO) and of  $1843 \text{ cm}^{-1}$  when the adsorbate layer saturates (the sample was exposed to about 10 Langmuir of NO) to a full coverage (see Figure 4.22). These new values correspond to linear iron nitrosyl compounds (Fe-N-O) [108–110] and indicate that NO molecules prefer to adsorb on the FeO(111)/Ag(100) system on top of iron atoms with molecular axis normal to the surface (see **Papers VII-IX**).

For a diatomic probe molecule approximated to a vibrating harmonic oscillator, which can also rigidly rotate, the expression for available energy levels is

$$E = \left(n + \frac{1}{2}\right)h\nu + \frac{h^2}{8\pi^2 I} j(j+1), (\Delta j = \pm 1, n = 0, 1, 2, \dots) \quad (4.18)$$

where  $n$  is the vibrational quantum number,  $h$  is the Planck constant,  $\nu$  is the vibration frequency,  $j$  is the rotational quantum number,  $I$  is the moment of inertia of the molecule. The vibrational frequency can be calculate as

$$\nu = \frac{1}{2\pi} \sqrt{\frac{k}{\mu}}; \frac{1}{\mu} = \frac{1}{m_1} + \frac{1}{m_2} \quad (4.19)$$

where  $k$  is the force constant of the vibrating molecular bond,  $m_1$  and  $m_2$  are the masses of the vibrating atoms.

When adsorbed on a surface, a molecule does not have rotational freedom any more and acts only as a vibrating oscillator. Besides, the frequency of vibrations changes due to the mechanical and chemical coupling to the substrate as well as the interaction of molecular dipole with the electric field of the surface in the case of polarizable metals [44]. The harmonic oscillator model is therefore somewhat crude as it does not take into account, e.g. a possible bond breaking or the anharmonicity of real bonds. For more physically realistic fitting of vibrational spectra other models like Morse or Lennard-Jones potentials and their

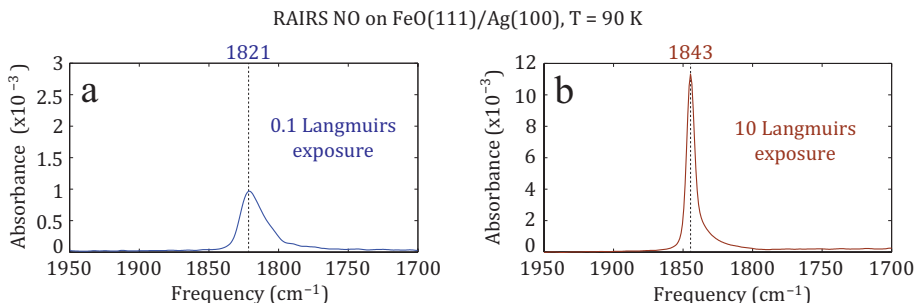


Figure 4.22: IR absorption spectra of NO adsorbed on the surface of a FeO(111)/Ag(100) system at a low coverage (0.1 Langmuire exposure) (a) and at saturation to a full coverage (10 Langmuire exposure) (b).

extensions can be applied. As the details of these theoretical models extend beyond the scope of the current work, the reader is referred to a related literature, e.g. Refs. [111–113].

While it is a difficult task to describe and model the vibrations of a molecule adsorbed on a surface, IR absorption spectra can be treated qualitatively with respect to known references as demonstrated with example of NO adsorption on FeO(111)/Ag(100).

#### 4.4.4 Temperature programmed desorption spectroscopy

In temperature programmed desorption spectroscopy the strength (i.e the bonding energy) of the adsorbate-substrate interactions is measured. For that purpose the sample with adsorbed molecules on the surface is heated with a constant heating rate in a UHV chamber. At a certain temperature the thermal energy transferred to the molecules becomes high enough to break the bonds and to promote desorption. This temperature is known as desorption temperature and its value can be determined by monitoring the gas concentration in the experimental chamber by a quadrupole mass spectrometer, which detects the molecules that have left the surface.

The binding energy varies with the combination of the adsorbate and the surface, and also with different types of adsorption sites. Therefore, one or several peaks of desorption at different temperatures may be observed with a QMS for a surface with molecules bound with the same or different strength respectively.

The analysis of TPD spectra yields several important parameters of an adsorbate, namely, the desorption activation energy, the strength of lateral interactions and the relative surface coverage of the adsorbate [100].

The activation energy of desorption can be described based on the Arrhenius equation:

$$r(\sigma) = -\frac{d\sigma}{dt} = \nu(\sigma)\sigma^n \cdot e^{-\frac{E_{acr}(\sigma)}{RT}} \quad (4.20)$$

where  $r(\sigma)$  is the desorption rate as a function of  $\sigma$  - the coverage,  $n$  is the order of desorption,  $\nu(\sigma)$  is the pre-exponential factor,  $E_{act}(\sigma)$  is the activation energy of desorption,  $R$  is the gas constant and  $T$  is the temperature.

This equation does not have a simple solution since several variables are coverage dependent and influence each other. Various approaches of TPD spectra analysis using different approximations are discussed by de Jong and Niemantsverdriet in Ref. [114]. The simplest "Redhead" method [115], for example, approximates equation 4.20 by making several assumptions. First, the pre-exponential factor and the activation energy are considered to be coverage independent. Second, the heating rate is linear. Third, no gases are adsorbed during the desorption process i.e. the system is retained under a perfect UHV, and no re-adsorption of the desorbed species occurs. As a result, for the first-order (atomic and simple molecular) and the second-order (recombinative molecular) desorption the activation energy can be determined from

$$\frac{E_{act}}{RT_m^2} = \frac{\nu_1}{\beta} \cdot e^{-\frac{E_{act}}{RT}}, \text{ for } n = 1 \quad (4.21)$$

$$\frac{E_{act}}{RT_m^2} = \frac{\sigma_0 \nu_2}{\beta} \cdot e^{-\frac{E_{act}}{RT}}, \text{ for } n = 2 \quad (4.22)$$

where  $T_m$  is the temperature value at which the desorption peak was recorded,  $\beta$  is the heating rate,  $\sigma_0$  is the area of the TPD peak, which is directly proportional to the surface coverage.

From equations 4.21 and 4.22 it is possible to iteratively determine  $E_{ads}$  starting with some initial value. The magnitudes of  $T_m$  and  $\beta$  are known from the experiment, while the pre-exponential factor is commonly assumed for  $n = 1$  to be on the order of the molecular vibration frequency,  $\sim 10^{13} \text{ s}^{-1}$ .

Lateral interactions within the adsorbate layer lead to lowering of adsorption energy and shifting of TPD peaks to the lower temperature values [100]. Thus, by analyzing the shift of the peaks and the corresponding decrease of the adsorption energy it is possible to determine the strength of lateral interactions between adsorbed molecules. The positions of TPD peaks, however, may depend on both coverage-dependent lateral interactions within the adsorbate layer and the potential presence of more than one type of adsorption sites, hence, in order to make certain conclusions it is necessary to obtain additional information about the molecules on the surface by means of a complementary experimental technique, e.g. RAIRS.

## 4.5 Theoretical calculations

### 4.5.1 Density functional theory

Density functional theory calculations are widely used for *ab initio* treatment of surface science problems [116]. This quantum-mechanical approach is based on the theoretical investigation of the nondegenerate lowest energy state (ground state) of the electronic structure of the system under the study.

The electronic structure may be determined by solving the Schrödinger equation

$$H\Psi = E\Psi \quad (4.23)$$

where  $H$  is the Hamiltonian,  $\Psi$  is the total wavefunction and  $E$  is the total energy of the system. However, due to the mutual dependence of all electronic wavefunctions, equation 4.23 does not have a direct solution and requires some approximation.

The original DFT and its later extensions are based on the Hohenberg-Kohn theorem [117], which suggests that the ground-state electron density  $n(\vec{r})$  in an external potential uniquely determines the effective potential of the system. It basically means that it is possible to treat an electronic system as an array of non-interacting particles existing in an external potential [118]. Hence, the total wavefunction  $\Psi$  can be viewed as a sum of independent wavefunctions for individual particles while the charge density of the system is maintained. Further, the problem of  $N$  bodies with  $3N$  spacial coordinates can be reduced by introduction of a functional of the electron density  $\Phi[n(\vec{r})]$ .

In order to determine the ground state, an iterative algorithm is used. It starts with calculation of the Hamiltonian for an initial eligible electron density. Further, the sequence of corrections is made by letting the electronic system relax in the calculations with corresponding corrections of the Hamiltonian after each iteration, until convergence is reached. The positions of atomic nuclei are also involved in the calculations, and thus, the atomic structure of the system can finally be determined. As theoretical calculations were not performed by the author personally, the readers are referred to Refs. [119–121] for more details of the DFT basics and applications.

It should be mentioned that the described calculations require a high computer power and are in many cases extremely time consuming. Thus, in order to resolve a structure, periodically repeated units of a reasonably small size should be considered.

### 4.5.2 STM simulation

The results of STM experiments, in many cases, don't give a direct answer to structural questions, since it is the electronic structure of a surface that is being imaged. Thus, in order to be able to analyze these results with a higher certainty, it is desirable to theoretically simulate the appearance of a surface as it is viewed by means of tunneling current. The problem that immediately arises with this task, however, is the unknown electronic structure of the tip.

The tunneling current in an STM experiment depends on the convolution of the electronic states of the surface and the tip. While it is relatively straightforward to model the electronic states of the sample surface, based on an eligible atomic model, it is impossible to know those of the tip, since every tip at any moment of time is unique and can not be controllably prepared. Thus, some universal model of the tip is required in order to avoid the uncertainty.

A suitable approximation allowing for theoretical modeling of STM images was implemented in the model developed by Tersoff and Hamann [122, 123], based on Bardeen's tunneling theory [124]. In this model the tip presence is introduced by a locally spherical potential placed at the end of the tip when it approaches the sample surface. The tunneling current is then proposed to be proportional to the surface local density of states (LDOS) at the Fermi level and spatially located under the center of the tip.

$$I \propto \rho(\vec{r}_0, E_F) \quad (4.24)$$

The STM image then represents a contour map of constant surface LDOS. For mathematical derivations and justifications of the model the readers are referred to the original paper of Tersoff and Hamann [123].

The discussed approximation allows for determination of the detailed electronic structure of the surface, while keeping the calculations computationally tractable. The main limitation of the model is the fact that the microscopic structure of the tip is completely ignored, which is currently unavoidable due to inability to control it during experiments.

# Summary of Papers

## High-energy surface X-ray diffraction studies of model Pd catalysts

The papers in this section report on *in situ* investigations of the structure of a Pd(100) ((**Papers I - IV**)) and a Pd(553) (**Paper V**) single crystal acting as model catalysts in the process of CO oxidation under semirealistic reaction conditions. The studies were performed using a novel experimental diffraction technique employing high-energy grazing X-ray radiation for fast determination of surface structures, while the CO<sub>2</sub> production was monitored by means of a quadrupole mass-spectrometer. Additionally, in **Paper III**, complementary STM, LEED and SXRD data were used.

Different surface structures were determined for different relative concentrations of CO and O<sub>2</sub>. In the case of Pd(100) heated to 600 K, the surface remains metallic in a CO rich gas mixture while the CO<sub>2</sub> production remains on a low level. When changing to a slightly oxygen rich gas mixture, the CO<sub>2</sub> production drastically increases indicating the activation of the catalyst and the HESXRD data show the presence of a Pd(100)-( $\sqrt{5} \times \sqrt{5}$ )R27°-PdO(101) surface oxide on the surface. After further increase of the oxygen partial pressure the surface oxide starts to grow in thickness following the Stranski-Krastanov growth mode and preserving the (101) crystallographic orientation. The growth continues until the registry with the substrate is lost and the film breaks into polycrystalline PdO. After reaction ignition, the CO<sub>2</sub> production remains at more or less the same level regardless of the current structure of the surface indicating a mass-transfer limited state of the catalyst. The surface recovers to its metallic state upon returning to CO rich conditions.

### **I – High-Energy Surface X-ray Diffraction for Fast Surface Structure Determination**

The first paper that was published within the scope of the current work introduces the HESXRD technique. It discusses and emphasizes the advantages of using high-energy X-rays in combination with a large area two-dimensional detector in surface diffraction experiments for a fast surface structure determination *in situ* under harsh conditions. The possibility to follow dynamic changes of the surface structure is also underlined. This novel

approach is described and illustrated by the studies of a Pd(100) single crystal surface acting like a catalyst during CO oxidation. The atomic structural model of the Pd(100)- $(\sqrt{5} \times \sqrt{5})R27^\circ$ -PdO(101) surface oxide is proposed and supported by the fitting of the experimental data.

## **II – Quantitative Surface Structure Determination Using In Situ High-Energy SXRD: Surface Oxide Formation on Pd(100) During Catalytic CO Oxidation**

The paper is devoted to the details of HESXRD experiment and data treatment. It complements **Paper I** with explanations of all corrections applied to the recorded diffraction patterns, the process of data analysis and computer software used for it. Three structural models for the epitaxial bulk oxide are compared in terms of their diffraction patterns and the Pd(100)- $(\sqrt{5} \times \sqrt{5})R27^\circ$ -PdO(101) structure is proved to be present on the surface in the catalytically active regime.

## **III – The Influence of Incommensurability on the Long Range periodicity of the Pd(100)- $(\sqrt{5} \times \sqrt{5})R27^\circ$ -PdO(101)**

The paper completes the *in situ* HESXRD structural studies of the one layer thick Pd(100)- $(\sqrt{5} \times \sqrt{5})R27^\circ$ -PdO(101) surface oxide forming on the surface of a Pd(100) single crystal when it is active towards catalytic CO oxidation under semirealistic reaction conditions. The results reported in **Papers I** and **II** are discussed in greater detail with the support of complementary STM, LEED and conventional SXRD data. Especially, the observed splitting of the diffraction rods in the recorded patterns is analyzed and attributed to the long-order incommensurability of the surface oxide and the substrate. The distortion of the  $(\sqrt{5} \times \sqrt{5})$  surface oxide unit cell and the formation of surface domains due to an accumulating lateral stress are discussed.

## **IV – Transient Structures of PdO During CO Oxidation Over Pd(100)**

The paper demonstrates the capability of HESXRD technique to resolve dynamic structural transformation of crystal surfaces. The change of a Pd(100) surface along with the changing reaction conditions during CO oxidation is discussed in detail. The structure of an epitaxial PdO(101) growing under slightly oxygen rich conditions is resolved and found to follow the Stranski-Krastanow mode of oxide growth. The morphology of the epitaxial oxide islands is analyzed quantitatively.

## **V – Step Dynamics and Oxide Formation During CO Oxidation over a Vicinal Pd Surface**

The paper reports on *in situ* HESXRD investigations of a Pd(553) single crystal during CO oxidation under semirealistic conditions. The surface structural transformations in the active catalytic regime are studied under static reaction conditions as well as under dynamic change in the gas partial pressure. A Pd(553) single crystal heated to 600 K in the gas mixture rich with CO was shown to preserve the metallic nature while upon increase of the oxygen partial pressure the surface becomes catalytically active and at the same time

undergoes restructuring into a combination of (332), (111) and (331) facets. It is very likely that a PdO(101) surface oxide structure is present on the (332) facets in this regime, as it was previously reported in the literature for Pd(553) exposed to pure oxygen. This conclusion is based on the fact that (332) facets dominate on the reconstructed surface while mass-spectrometry shows a high rate of the CO<sub>2</sub> production. With further increase of the oxygen partial pressure the surface becomes covered with a thick polycrystalline PdO. The surface rapidly recovers, however, to the initial Pd(553) structure upon returning to CO rich conditions. Additionally, the dynamic measurements show the formation of several oxygen adsorbate structures upon the sample catalytic activation and before the complete surface restructuring.

## Multitechnique studies of ultrathin iron oxide films

The papers in this section report on the structural and NO adsorption properties of ultrathin iron oxide films grown on a Ag(100) and a Ag(111) single crystal substrates. The investigations were performed by means of several experimental techniques as well as theoretical calculations. The results show that it is possible to grow films of different thicknesses, structure and stoichiometry by reactive deposition of iron in oxygen atmosphere on a substrate varying the preparation conditions (**Paper VI**). For FeO(111) films grown on both Ag substrates it was shown that NO molecules readily adsorb on the iron ions of the surface at 100 K forming a dense monolayer (**Papers VII and IX**). The molecular axis of adsorbed molecules is normal to the surface. The comparison of these results with the results reported in the literature for similar films grown on Pt(111) where NO uptake is negligible at the same temperature allowed us to conclude that the structural effects greatly affect the adsorption properties of the films. Namely, for the smaller FeO unit cell in the case of the Pt(111) the rumpling of the film is greater, causing the oxygen atoms to protrude and to sterically block the iron ions. Besides, it was shown that the NO binding energy varies markedly for different charge states and local environment of Fe ions (**Paper VIII**). The Fe<sup>2+</sup> ions namely bind NO more strongly than the Fe<sup>3+</sup> ions. At the same time the N–O stretch frequency measured by RAIRS is relatively insensitive to the charge of iron ions, which suggests that  $\pi$ -backbonding of NO adsorbed species does not differ significantly between different Fe sites and that other factors are responsible for the difference in the binding energy.

### VI – Growth of Ultrathin Iron Oxide Films on Ag(100)

The paper focuses on the preparation and structural characterization of FeO films with different thickness, structure and stoichiometry grown by reactive deposition of iron in oxygen atmosphere on a Ag(100) single crystal surface. The STM, LEED and complementary XPS structural studies are reported for films prepared under different growth conditions. The obtained one layer thick FeO(111) films, as well as multilayer FeO<sub>x</sub>, are investigated and the

structural models for the observed iron oxide films are proposed.

### **VII – Fe Oxides on Ag Surfaces: Structure and Reactivity**

The paper compares the structural and NO adsorption properties of one layer thick FeO(111) films grown on a Ag(100) and a Ag(111) single crystal surface. The surface unit cell dimensions are found from STM, LEED and SXRD experimental data. The atomic structural model of FeO(111)/Ag(100) is proposed and supported by the fitting of SXRD experimental results. The NO adsorption properties of both systems are studied by means of TPD, RAIRS and theoretical calculations and compared with the data reported for FeO(111)/Pt(111) reported in the literature.

### **VIII – Adsorption of NO on FeO<sub>x</sub> Films Grown on Ag(111)**

The paper reports on combined TPD and RAIRS studies of the NO adsorption properties of FeO<sub>x</sub> films grown on a Ag(111) single crystal substrate. The results are obtained for one layer thick FeO(111) films, Fe<sub>3</sub>O<sub>4</sub>(111) layer and FeO<sub>x</sub> multilayer structures. It is shown that NO molecules bind to Fe ions with the molecular axis normal to the surface. It is also found that the NO binding energy varies markedly for different charge states and local environment of Fe ions and the factors responsible for the difference in the binding energy are discussed.

### **IX – Tuning the Reactivity of Ultrathin Oxides: NO Adsorption on Monolayer FeO(111)**

The paper reports on STM, LEED, TPD and RAIRS experimental studies of the interplay between NO adsorption properties of an FeO(111) monolayer and its structure on various substrates. The experimental observations are supported by theoretical calculations. Two systems with drastically different adsorption properties were compared and analyzed in detail, namely FeO(111)/Ag(100) and FeO(111)/Pt(111). The results of the theoretical calculations indicate that the adsorbed states are nearly identical on both systems while experimental observation show a clear difference. The conclusion is made that the drastic difference in adsorption properties is a purely structural effect caused by a greater rumpling of the iron oxide layer on the Pt(111) substrate where, due to the smaller unit cell, oxygen atoms are pulled outwards blocking the iron ions for adsorption.

# Conclusions and Outlook

The structural studies of catalytically active materials under reaction conditions are of a great importance for the improvement of existing approaches in heterogeneous catalysis as well as for the development of new functional materials. In the present work we have performed a multitechnique investigation of Pd-based model catalysts and FeO ultrathin films grown on Ag(100) and Ag(111) single crystal substrates. The obtained results are valuable for the fundamental understanding of the atomic processes occurring on the surface of a working catalyst and of the interplay between the structural and physical properties of thin films.

We have developed and employed a novel technique of high-energy surface X-ray diffraction, which allowed us to perform investigations *in situ* and under realistic reaction conditions. This approach delivers a solution for the pressure gap problem in the studies of heterogeneous catalysts. Besides that, it allows for fast determination of the surface structure, which is extremely important in the cases when dynamic processes occur on the surface. A data analysis procedure, which was not available before, was developed and successfully applied to several data sets obtained while studying Pd-based model catalysts in the process of CO oxidation.

The future perspectives related to the present work are quite broad. First of all, the developed experimental approach and data analysis procedure for HESXRD allow us to concentrate on the investigations of unknown surface structures related to heterogeneous catalysis. More materials as well as more surface orientations may be studied to increase the understanding of catalytic processes on the atomic scale occurring under realistic reaction conditions. In addition to the studies reported in this dissertation, we have, in fact, performed *in situ* measurements of several other systems. These data should be analyzed and the observed surface structures should be resolved in the future.

The other potential aim is to combine the developed experimental approach with other techniques to perform more comprehensive investigations. Such an attempt was successfully made in August 2016 at the P07 beamline at Petra III. We performed combined high-energy surface X-ray diffraction and planar laser induced fluorescence [125, 126] measurements of a Pd(100) single crystal surface acting like a model catalyst for CO oxidation. It

allowed us to monitor the dynamics of the surface structure simultaneously with the gas distribution over the surface, thus delivering insight into the reaction kinetics.



Figure C1: A photo of warning signs enabled during the experiments combining high-energy surface X-ray diffraction and laser induced planar fluorescence at P07 beamline of Petra III in August 2016.

The studies of the structural and the adsorption properties of ultra-thin films grown on various substrates shall also be continued. The next potential step is to study the adsorption properties of well ordered several-layers thick iron oxide films grown on Ag and Pt substrates in more detail. In particular, it would be interesting to study similar FeO films grown on Ag(111) and Pt(111) *in situ* at semirealistic conditions to compare the influence of the substrate on the reactivity. In general, the behavior and unique catalytic properties of such thin oxide films under semirealistic conditions is an unexplored area in the field of surface science.

# Bibliography

- [1] J. J. Berzelius. *Einige Ideen über eine bei der Bildung organischer Verbindungen in der lebenden Natur wirksame, aber bisher nicht bemerkte Kraft*. Jahres-Berkcht über die Fortschritte der Chemie 15, pp. 237–245, **1836**.
- [2] G. Ertl. *Reactions at Surfaces: From Atoms to Complexity (Nobel Lecture)*. Angewandte Chemie International Edition 47(19), pp. 3524–3535, **2008**. doi:10.1002/anie.200800480.
- [3] W. Ostwald. *Catalysis*. Physikalische Zeitschrift 3, pp. 313–322, **1901**.
- [4] H.-J. Freund, G. Meijer, M. Scheffler, R. Schlögl, and M. Wolf. *CO oxidation as a prototypical reaction for heterogeneous processes*. Angewandte Chemie International Edition 50(43), pp. 10064–10094, **2011**. doi:10.1002/anie.201101378.
- [5] I. Langmuir. *The mechanism of the catalytic action of platinum in the reactions  $2CO + O_2 = 2CO_2$  and  $2H_2 + O_2 = 2H_2O$* . Transactions of the Faraday Society 17, pp. 621–654, **1922**.
- [6] T. Engel and G. Ertl. *Elementary Steps in the Catalytic Oxidation of Carbon Monoxide on Platinum Metals*. Advances in Catalysis 28, pp. 1 – 78, **1979**. doi:10.1016/S0360-0564(08)60133-9.
- [7] G. Ertl, H. Knözinger, F. Schüth, and J. Weitkamp. *Handbook of heterogeneous catalysis: 8 volumes*. wiley-vch, **2008**.
- [8] F. Gao, Y. Wang, Y. Cai, and D. W. Goodman. *CO Oxidation on Pt-Group Metals from Ultrahigh Vacuum to Near Atmospheric Pressures. 2. Palladium and Platinum*. The Journal of Physical Chemistry C 113(1), pp. 174–181, **2009**. doi:10.1021/jp8077985.
- [9] R. van Rijn, O. Balmes, R. Felici, J. Gustafson, D. Wermeille, R. Westerström, E. Lundgren, and J. W. M. Frenken. *Comment on “CO Oxidation on Pt-Group Metals from Ultrahigh Vacuum to Near Atmospheric Pressures. 2. Palladium and Platinum”*.

- The Journal of Physical Chemistry C 114(14), pp. 6875–6876, **2010**. doi:10.1021/jp911406x.
- [10] F. Gao, Y. Wang, and D. W. Goodman. *Reply to “Comment on “CO Oxidation on Pt-Group Metals from Ultrahigh Vacuum to Near Atmospheric Pressures. 2. Palladium and Platinum”*. The Journal of Physical Chemistry C 114(14), pp. 6874–6874, **2010**. doi:10.1021/jp100134e.
- [11] R. van Rijn, O. Balmes, A. Resta, D. Wermeille, R. Westerström, J. Gustafson, R. Felici, E. Lundgren, and J. W. M. Frenken. *Surface structure and reactivity of Pd(100) during CO oxidation near ambient pressures*. Physical Chemistry Chemical Physics 13, pp. 13167–13171, **2011**. doi:10.1039/C1CP20989B.
- [12] S. Blomberg, M. J. Hoffmann, J. Gustafson, N. M. Martin, V. R. Fernandes, A. Borg, Z. Liu, R. Chang, S. Matera, K. Reuter, and E. Lundgren. *In Situ X-Ray Photoelectron Spectroscopy of Model Catalysts: At the Edge of the Gap*. Physical Review Letters 110, p. 117601, **2013**. doi:10.1103/PhysRevLett.110.117601.
- [13] S. A. Chambers. *Epitaxial growth and properties of thin film oxides*. Surface Science Reports 39(5-6), pp. 105 – 180, **2000**. doi:10.1016/S0167-5729(00)00005-4.
- [14] G. S. Parkinson. *Iron oxide surfaces*. Surface Science Reports 71(1), pp. 272 – 365, **2016**. doi:10.1016/j.surfrep.2016.02.001.
- [15] D. Schlom, J. Haeni, J. Lettieri, C. Theis, W. Tian, J. Jiang, and X. Pan. *Oxide nano-engineering using MBE*. Materials Science and Engineering: B 87(3), pp. 282 – 291, **2001**. doi:10.1016/S0921-5107(01)00726-7.
- [16] S. Surnev, A. Fortunelli, and F. P. Netzer. *Structure–Property Relationship and Chemical Aspects of Oxide–Metal Hybrid Nanostructures*. Chemical Reviews 113(6), pp. 4314–4372, **2013**. doi:10.1021/cr300307n.
- [17] G. Pacchioni. *Two-Dimensional Oxides and Their Role in Electron Transfer Mechanisms with Adsorbed Species*. The Chemical Record 14(5), pp. 910–922, **2014**. doi:10.1002/tcr.201402002.
- [18] W. Weiss and W. Ranke. *Surface chemistry and catalysis on well-defined epitaxial iron-oxide layers*. Progress in Surface Science 70(1 - 3), pp. 1 – 151, **2002**. doi:10.1016/S0079-6816(01)00056-9.
- [19] Y. Lei, M. Lewandowski, Y.-N. Sun, Y. Fujimori, Y. Martynova, I. M. N. Groot, R. J. Meyer, L. Giordano, G. Pacchioni, J. Goniakowski, C. Noguera, S. Shaikhutdinov, and H.-J. Freund. *CO+NO versus CO+O<sub>2</sub> Reaction on Monolayer FeO(111) Films on Pt(111)*. ChemCatChem 3(4), pp. 671–674, **2011**. doi:10.1002/cctc.201000388.

- [20] N. Greenwood and A. Earnshaw. *Chemistry of the Elements 2nd Edition*. Butterworth-Heinemann, 1997.
- [21] T. Hahn, ed. *International Tables for Crystallography. Volume A: Space-group symmetry. Online edition*. International Union of Crystallography, 2006. doi:10.1107/97809553602060000100.
- [22] C. Giacovazzo, ed. *Fundamentals of Crystallography*. Oxford University Press, 1992.
- [23] J. A. Appelbaum, G. A. Baraff, and D. R. Hamann. *The Si (100) surface. III. Surface reconstruction*. Physical Review B 14, pp. 588–601, 1976. doi:10.1103/PhysRevB.14.588.
- [24] Z. Jing and J. L. Whitten. *Ab initio studies of Si(100) surface reconstruction*. Surface Science 274(1), pp. 106 – 112, 1992. doi:10.1016/0039-6028(92)90104-E.
- [25] G. W. Brown, H. Grube, M. E. Hawley, S. R. Schofield, N. J. Curson, M. Y. Simmons, and R. G. Clark. *Imaging charged defects on clean Si(100)-(2×1) with scanning tunneling microscopy*. Journal of Applied Physics 92(2), pp. 820–824, 2002. doi:10.1063/1.1486047.
- [26] G. A. Somorjai and Y. Li. *Introduction to surface chemistry and catalysis*. John Wiley & Sons, 2010.
- [27] M. Batzill and U. Diebold. *The surface and materials science of tin oxide*. Progress in Surface Science 79(2-4), pp. 47 – 154, 2005. doi:10.1016/j.progsurf.2005.09.002.
- [28] A. Beltrán, J. Andrés, E. Longo, and E. R. Leite. *Thermodynamic argument about SnO<sub>2</sub> nanoribbon growth*. Applied Physics Letters 83(4), pp. 635–637, 2003. doi:10.1063/1.1594837.
- [29] D. F. Cox, T. B. Fryberger, and S. Semancik. *Oxygen vacancies and defect electronic states on the SnO<sub>2</sub>(110)-(1×1) surface*. Physical Review B 38, pp. 2072–2083, 1988. doi:10.1103/PhysRevB.38.2072.
- [30] F. Jones, R. Dixon, J. Foord, R. Egdell, and J. Pethica. *The surface structure of SnO<sub>2</sub>(110)-(4×1) revealed by scanning tunneling microscopy*. Surface Science 376(1), pp. 367 – 373, 1997. doi:10.1016/S0039-6028(96)01327-1.
- [31] E. de Frésart, J. Darville, and J. Gilles. *Surface reconstructions of the SnO<sub>2</sub>(110) face*. Solid State Communications 37(1), pp. 13 – 17, 1981. doi:10.1016/0038-1098(81)90879-6.
- [32] E. de Frésart, J. Darville, and J. Gilles. *Influence of the surface reconstruction on the work function and surface conductance of (110) SnO<sub>2</sub>*. Applications of Surface Science 11, pp. 637–651, 1982. doi:10.1016/0378-5963(82)90109-X.

- [33] E. De Frésart, J. Darville, and J. Gilles. *Surface properties of tin dioxide single crystals*. Surface Science 126(1-3), pp. 518–522, **1983**. doi:10.1016/0039-6028(83)90751-3.
- [34] R. Egdell, S. Eriksen, and W. Flavell. *Oxygen deficient SnO<sub>2</sub>(110) and TiO<sub>2</sub>(110): A comparative study by photoemission*. Solid State Communications 60(10), pp. 835–838, **1986**. doi:10.1016/0038-1098(86)90607-1.
- [35] D. F. Cox, T. B. Fryberger, and S. Semancik. *Surface reconstructions of oxygen deficient SnO<sub>2</sub>(110)*. Surface Science 224(1-3), pp. 121–142, **1989**. doi:10.1016/0039-6028(89)90905-9.
- [36] J. Themlin, R. Sporken, J. Darville, R. Caudano, J. Gilles, and R. Johnson. *Resonant-photoemission study of SnO<sub>2</sub>: cationic origin of the defect band-gap states*. Physical Review B 42(18), p. 11914, **1990**. doi:10.1103/PhysRevB.42.11914.
- [37] C. Pang, S. Haycock, H. Raza, P. Møller, and G. Thornton. *Structures of the 4×1 and 1×2 reconstructions of SnO<sub>2</sub>(110)*. Physical Review B 62(12), p. R7775, **2000**. doi:10.1103/PhysRevB.62.R7775.
- [38] M. Sinner-Hettenbach, M. Göthelid, J. Weissenrieder, H. von Schenck, T. Weiß, N. Barsan, and U. Weimar. *Oxygen-deficient SnO<sub>2</sub>(110): a STM, LEED and XPS study*. Surface Science 477(1), pp. 50–58, **2001**. doi:10.1016/S0039-6028(01)00705-1.
- [39] A. Atrei, E. Zanazzi, U. Bardi, and G. Rovida. *The SnO<sub>2</sub>(110)-(4×1) structure determined by LEED intensity analysis*. Surface Science 475(1), pp. L223–L228, **2001**. doi:10.1016/S0039-6028(00)01044-X.
- [40] M. A. Mäki-Jaskari and T. T. Rantala. *Theoretical study of oxygen-deficient SnO<sub>2</sub>(110) surfaces*. Physical Review B 65(24), p. 245428, **2002**. doi:10.1103/PhysRevB.65.245428.
- [41] J. Oviedo and M. Gillan. *Reconstructions of strongly reduced SnO<sub>2</sub>(110) studied by first-principles methods*. Surface Science 513(1), pp. 26–36, **2002**. doi:10.1016/S0039-6028(02)01725-9.
- [42] M. Batzill, K. Katsiev, and U. Diebold. *Surface morphologies of SnO<sub>2</sub>(110)*. Surface Science 529(3), pp. 295–311, **2003**. doi:10.1016/S0039-6028(03)00357-1.
- [43] P. Ágoston and K. Albe. *Disordered reconstructions of the reduced SnO<sub>2</sub>-(110) surface*. Surface Science 605(7-8), pp. 714 – 722, **2011**. doi:10.1016/j.susc.2011.01.007.
- [44] I. Chorkendorff and J. W. Niemantsverdriet. *Concepts of Modern Catalysis and Kinetics*. Wiley-VCH Verlag GmbH & Co. KGaA, **2005**. doi:10.1002/3527602658.fmatter.

- [45] R. I. Masel. *Principles of adsorption and reaction on solid surfaces*, vol. 3. John Wiley & Sons, 1996.
- [46] J. E. Lennard-Jones. *On the determination of molecular fields. II. From the equation of state of a gas*. Proceedings of the Royal Society of London A: Mathematical, Physical and Engineering Sciences 106(738), pp. 463–477, 1924.
- [47] J. Lennard-Jones. *Processes of adsorption and diffusion on solid surfaces*. Transactions of the Faraday Society 28, pp. 333–359, 1932.
- [48] M. Bowker. *The basis and applications of heterogeneous catalysis*. Oxford University Press, 1998.
- [49] A. B. Ray and F. O. Andereg. *The oxidation of carbon monoxide by passage with oxygen or air through the silent discharge and over ozone decomposing catalysts*. Journal of the American Chemical Society 43(5), pp. 967–978, 1921. doi:10.1021/ja01438a001.
- [50] J. A. Dumesic, G. W. Huber, and M. Boudart. *Principles of heterogeneous catalysis*. Handbook of Heterogeneous Catalysis 2008. doi:10.1002/9783527610044.hetcat0001.
- [51] D. D. Eley and E. K. Rideal. *Parahydrogen Conversion on Tungsten*. Nature (146), pp. 401–402, 1940. doi:10.1038/146401d0.
- [52] J. T. Hirvi, T.-J. J. Kinnunen, M. Suvanto, T. A. Pakkanen, and J. K. Nørskov. *CO oxidation on PdO surfaces*. The Journal of Chemical Physics 133(8), 2010. doi:10.1063/1.3464481.
- [53] P. Mars and D. W. van Krevelen. *Oxidations carried out by means of vanadium oxide catalysts*. Chemical Engineering Science 3, pp. 41–59, 1954. doi:10.1016/S0009-2509(54)80005-4.
- [54] Y.-N. Sun, Z.-H. Qin, M. Lewandowski, E. Carrasco, M. Sterrer, S. Shaikhutdinov, and H.-J. Freund. *Monolayer iron oxide film on platinum promotes low temperature {CO} oxidation*. Journal of Catalysis 266(2), pp. 359 – 368, 2009. doi:10.1016/j.jcat.2009.07.002.
- [55] Y.-N. Sun, L. Giordano, J. Goniakowski, M. Lewandowski, Z.-H. Qin, C. Noguera, S. Shaikhutdinov, G. Pacchioni, and H.-J. Freund. *The Interplay between Structure and CO Oxidation Catalysis on Metal-Supported Ultrathin Oxide Films*. Angewandte Chemie International Edition 49(26), pp. 4418–4421, 2010. doi:10.1002/anie.201000437.
- [56] K. Reuter, M. V. Ganduglia-Pirovano, C. Stampfl, and M. Scheffler. *Metastable precursors during the oxidation of the Ru(0001) surface*. Physical Review B 65, p. 165403, 2002. doi:10.1103/PhysRevB.65.165403.

- [57] M. Todorova, W. X. Li, M. V. Ganduglia-Pirovano, C. Stampfl, K. Reuter, and M. Scheffler. *Role of Subsurface Oxygen in Oxide Formation at Transition Metal Surfaces*. Physical Review Letters 89, p. 096103, **2002**. doi:10.1103/PhysRevLett.89.096103.
- [58] K. R. Lawless. *The oxidation of metals*. Reports on Progress in Physics 37(2), p. 231, **1974**.
- [59] E. Lundgren, A. Mikkelsen, J. N. Andersen, G. Kresse, M. Schmid, and P. Varga. *Surface oxides on close-packed surfaces of late transition metals*. Journal of Physics: Condensed Matter 18(30), p. R481, **2006**.
- [60] J. F. Weaver. *Surface Chemistry of Late Transition Metal Oxides*. Chemical Reviews 113(6), pp. 4164–4215, **2013**. doi:10.1021/cr300323w.
- [61] J. Y. Park, K. Qadir, and S. M. Kim. *Role of Surface Oxides on Model Nanocatalysts in Catalytic Activity of CO Oxidation*, pp. 145–170. Springer New York, New York, NY, **2014**. doi:10.1007/978-1-4614-8742-5\_7.
- [62] A. Asthagiri, D. A. Dixon, Z. Dohnálek, B. D. Kay, J. A. Rodriguez, R. Rousseau, D. J. Stacchiola, and J. F. Weaver. *Catalytic Chemistry on Oxide Nanostructures*, pp. 251–280. Springer International Publishing, **2016**. doi:10.1007/978-3-319-28332-6\_9.
- [63] J. Choi, L. Pan, V. Mehar, F. Zhang, A. Asthagiri, and J. F. Weaver. *Promotion of CO oxidation on PdO(101) by adsorbed H<sub>2</sub>O*. Surface Science 650, pp. 203 – 209, **2016**. doi:10.1016/j.susc.2015.08.043.
- [64] E. Lundgren, G. Kresse, C. Klein, M. Borg, J. N. Andersen, M. De Santis, Y. Gauthier, C. Konvicka, M. Schmid, and P. Varga. *Two-Dimensional Oxide on Pd(111)*. Physical Review Letters 88, p. 246103, **2002**. doi:10.1103/PhysRevLett.88.246103.
- [65] R. Franchy. *Growth of thin, crystalline oxide, nitride and oxynitride films on metal and metal alloy surfaces*. Surface Science Reports 38(6-8), pp. 195 – 294, **2000**. doi:10.1016/S0167-5729(99)00013-8.
- [66] W. Friedrich, P. Knipping, and M. Laue. *Interferenz-Erscheinungen bei Röntgenstrahlen Sitzungsber. Kgl. Bayer: Akad. Wiss 303*, **1912**.
- [67] W. H. Bragg and W. L. Bragg. *The Reflection of X-rays by Crystals*. Proceedings of the Royal Society of London A: Mathematical, Physical and Engineering Sciences 88(605), pp. 428–438, **1913**. doi:10.1098/rspa.1913.0040.
- [68] W. C. Marra, P. Eisenberger, and A. Y. Cho. *X-ray Total-External-Reflection-Bragg Diffraction: A Structural Study of the GaAs-Al Interface*. Journal of Applied Physics 50(11), pp. 6927–6933, **1979**. doi:10.1063/1.325845.

- [69] P. Willmott. *An introduction to synchrotron radiation: Techniques and applications*. John Wiley & Sons Ltd, 2011. doi:10.1002/9781119970958.
- [70] N. W. Ashcroft and N. D. Mermin. *Solid state physics*. Holt, Rinehart and Winston, Philadelphia, USA, 1976.
- [71] P. Eisenberger and W. C. Marra. *X-Ray Diffraction Study of the Ge(001) Reconstructed Surface*. Physical Review Letters 46, pp. 1081–1084, 1981. doi:10.1103/PhysRevLett.46.1081.
- [72] A. M. Afanas'ev, P. A. Aleksandrov, R. M. Imamov, A. A. Lomov, and A. A. Zavyalova. *Diffraction scattering at angles far from the Bragg angle and the structure of thin subsurface layers*. Acta Crystallographica A A40, pp. 352–355, 1984. doi:10.1107/S0108767384000763.
- [73] C. A. Lucas, E. Gartstein, and R. A. Cowley. *The resolution function of an X-ray triple-crystal diffractometer: comparison of experiment and theory*. Acta Crystallographica A A45, pp. 416–422, 1989. doi:10.1107/S010876738900108X.
- [74] I. K. Robinson, R. T. Tung, and R. Feidenhans'l. *X-ray interference method for studying interface structures*. Physical Review B 38, pp. 3632–3635, 1988. doi:10.1103/PhysRevB.38.3632.
- [75] E. Vlieg, J. V. D. Veen, S. Gurman, C. Norris, and J. Macdonald. *X-ray diffraction from rough, relaxed and reconstructed surfaces*. Surface Science 210(3), pp. 301 – 321, 1989. doi:10.1016/0039-6028(89)90598-0.
- [76] R. Feidenhans'l. *Surface structure determination by X-ray diffraction*. Surface Science Reports 10(3), pp. 105 – 188, 1989. doi:10.1016/0167-5729(89)90002-2.
- [77] E. Vlieg. *Integrated Intensities Using a Six-Circle Surface X-ray Diffractometer*. Journal of Applied Crystallography 30, pp. 532–543, 1997. doi:10.1107/S0021889897002537.
- [78] C. M. Schlepütz, S. O. Mariager, S. A. Pauli, R. Feidenhans'l, and P. R. Willmott. *Angle calculations for a (2+3)-type diffractometer: focus on area detectors*. Journal of Applied Crystallography 44, pp. 73–83, 2011. doi:10.1107/S0021889810048922.
- [79] J. Drnec, T. Zhou, S. Pintea, W. Onderwaater, E. Vlieg, G. Renaud, and R. Felici. *Integration techniques for surface X-ray diffraction data obtained with a two-dimensional detector*. Journal of Applied Crystallography 47, pp. 365–377, 2014. doi:10.1107/S1600576713032342.
- [80] M. Shipilin. *High-energy SXRD for in situ surface structure determination*, **Licentiate thesis**, 2014.

- [81] I. Robinson. *Crystal truncation rods and surface roughness*. Physical Review B 33(6), p. 3830, **1986**. doi:10.1103/PhysRevB.33.3830.
- [82] N. Schell, A. King, F. Beckmann, H.-U. Ruhnau, R. Kirchhof, R. Kiehn, M. Müller, A. Schreyer, R. Garrett, I. Gentle, *et al.* *The high energy materials science beamline (HEMS) at PETRA III*. AIP Conference Proceedings 1234(1), p. 391, **2010**.
- [83] *I07: Surface and interface diffraction*. <http://www.diamond.ac.uk/I07>.
- [84] C. Davisson and L. H. Germer. *Diffraction of Electrons by a Crystal of Nickel*. Physical Review 30, pp. 705–740, **1927**. doi:10.1103/PhysRev.30.705.
- [85] H. E. Farnsworth. *Penetration of Low Speed Diffracted Electrons*. Physical Review 49, pp. 605–609, **1936**. doi:10.1103/PhysRev.49.605.
- [86] F. Jona. *LEED Crystallography*. Journal of Physics C: Solid State Physics 11(21), pp. 4271–4306, **1978**.
- [87] K. Heinz. *LEED and DLEED as Modern Tools for Quantitative Surface Structure Determination*. Reports on Progress in Physics 58(6), pp. 637–704, **1995**.
- [88] M. Horn-von Hoegen. *Growth of semiconductor layers studied by spot profile analysing low energy electron diffraction - Part II*. Zeitschrift für Kristallographie 214(11), pp. 684–721, **1999**. doi:10.1524/zkri.1999.214.11.684.
- [89] M. P. Seah and W. A. Dench. *Quantitative electron spectroscopy of surfaces: A standard data base for electron inelastic mean free paths in solids*. Surface and Interface Analysis 1(1), pp. 2–11, **1979**. doi:10.1002/sia.740010103.
- [90] C. D. Wagner, L. E. Davis, and W. M. Riggs. *The energy dependence of the electron mean free path*. Surface and Interface Analysis 2(2), pp. 53–55, **1980**. doi:10.1002/sia.740020204.
- [91] S. Tanuma, C. J. Powell, and D. R. Penn. *Calculations of electron inelastic mean free paths (IMFPS). IV. Evaluation of calculated IMFPS and of the predictive IMFP formula TPP-2 for electron energies between 50 and 2000 eV*. Surface and Interface Analysis 20(1), pp. 77–89, **1993**. doi:10.1002/sia.740200112.
- [92] M. Horn-von Hoegen. *Growth of semiconductor layers studied by spot profile analysing low energy electron diffraction*. Zeitschrift für kristallographie 214(10), pp. 591–629, 684–721, **1999**.
- [93] G. Binnig, H. Rohrer, C. Gerber, and E. Weibel. *Tunneling through a controllable vacuum gap*. Applied Physics Letters 40(2), pp. 178–180, **1982**. doi:10.1063/1.92999.

- [94] G. Binnig and H. Rohrer. *Scanning tunneling microscopy*. Surface Science 126(1), pp. 236 – 244, **1983**. doi:10.1016/0039-6028(83)90716-1.
- [95] P. W. Hawkes and J. C. H. Spence. *Science of microscopy*. Springer Science+Business Media, LLC, New York, USA, **2007**.
- [96] A. Einstein. *Über einen die Erzeugung und Verwandlung des Lichtes betreffenden heuristischen Gesichtspunkt*. Annalen der Physik 322, pp. 132–148, **1905**. doi:10.1002/andp.19053220607.
- [97] N. Mårtensson, P. Baltzer, P. Brühwiler, J.-O. Forsell, A. Nilsson, A. Stenborg, and B. Wannberg. *A very high resolution electron spectrometer*. Journal of Electron Spectroscopy and Related Phenomena 70(2), pp. 117–128, **1994**. doi:10.1016/0368-2048(94)02224-N.
- [98] H. Bubert, J. C. Rivière, H. F. Arlinghaus, H. Hutter, H. Jenett, P. Bauer, L. Palmetshofer, L. Fabry, S. Pahlke, A. Quentmeier, K. Hinrichs, W. Hill, B. Gruska, A. Röseler, and G. Friedbacher. *Surface and Thin Film Analysis*. Wiley-VCH, Weinheim - Germany, **2000**. doi:10.1002/14356007.b06\023.
- [99] C. Wagner, W. Riggs, L. Davis, J. Moulder, and G. Muilenberg. *Handbook of X-ray Photoelectron Spectroscopy*. Perkin-Elmer Corporation: Eden Prairie, MN, USA, **1979**.
- [100] G. Attard and C. Barnes. *Surfaces*. Oxford university press, **2011**.
- [101] A. Thompson, ed. *X-ray Data Booklet*. Lawrence Berkeley National Laboratory, University of California, Berkeley, CA, USA, **2009**.
- [102] D. King and D. Woodruff, eds. *The chemical physics of solid surfaces and heterogeneous catalysis*, vol. 2. Elsevier, Amsterdam, **1983**.
- [103] N. Martin. *Surface Studies of Model Systems Relevant for Pd and Ag Catalysts*. Ph.D. thesis, Lund University, **2014**.
- [104] L. C. Feldman and J. W. Mayer. *Fundamentals of Surface Thin Film Analysis*. Pearson Education (US), **1986**.
- [105] R. P. Eischens and W. A. Pliskin. *The Infrared Spectra of Adsorbed Molecules*. Advances in Catalysis 10, pp. 1 – 56, **1958**. doi:10.1016/S0360-0564(08)60403-4.
- [106] E. B. Wilson, J. C. Decius, and C. P. C. *Molecular vibrations : the theory of infrared and Raman vibrational spectra*. New York : McGraw-Hill, **1955**.

- [107] F. M. Hoffmann. *Infrared reflection-absorption spectroscopy of adsorbed molecules*. Surface Science Reports 3(2), pp. 107 – 192, 1983. doi:10.1016/0167-5729(83)90001-8.
- [108] J. A. Ibers and D. M. P. Mingos. *Crystal and molecular structure of hydridonitrosyltris(triphenylphosphine)iridium(I) perchlorate,  $[IrH(NO)(P(C_6H_5)_3)_3][ClO_4]$* . Inorganic Chemistry 10(7), pp. 1479–1486, 1971. doi:10.1021/ic50101a033.
- [109] A. P. Gaughan, B. L. Haymore, J. A. Ibers, W. H. Myers, T. E. Nappier, and D. W. Meek. *Extension of the nitrosyl-aryldiazo analogy. Structure of an aryldiazo group coordinated to rhodium in a doubly bent fashion*. Journal of the American Chemical Society 95(20), pp. 6859–6861, 1973. doi:10.1021/ja00801a070.
- [110] B. L. Haymore and J. A. Ibers. *Comparison of linear nitrosyl and singly bent aryldiazo complexes of ruthenium. Structures of trichloronitrosylbis(triphenylphosphine)ruthenium,  $RuCl_3(NO)(P(C_6H_5)_3)_2$ , and trichloro(p-tolyl)diazobis(triphenylphosphine)ruthenium-dichloromethane,  $RuCl_3(p-NNC_6H_4CH_3)(P(C_6H_5)_3)_2 \cdot CH_2Cl_2$* . Inorganic Chemistry 14(12), pp. 3060–3070, 1975. doi:10.1021/ic50154a041.
- [111] J. Atkins Peter, de Paula. *Atkins' Physical Chemistry, 10th edition*. Oxford University Press, Oxford, 2014.
- [112] J. P. Dahl and M. Springborg. *The Morse oscillator in position space, momentum space, and phase space*. The Journal of Chemical Physics 88(7), pp. 4535–4547, 1988. doi:10.1063/1.453761.
- [113] R. J. Le Roy, N. S. Dattani, J. A. Coxon, A. J. Ross, P. Crozet, and C. Linton. *Accurate analytic potentials for  $Li_2(X^1\Sigma_g^+)$  and  $Li_2(A^1\Sigma_u^+)$  from 2 to 90°, and the radiative lifetime of  $Li(2p)$* . The Journal of Chemical Physics 131(20), pp. 204309–1 – 204309–17, 2009. doi:10.1063/1.3264688.
- [114] A. de Jong and J. Niemantsverdriet. *Thermal desorption analysis: Comparative test of ten commonly applied procedures*. Surface Science 233(3), pp. 355 – 365, 1990. doi:10.1016/0039-6028(90)90649-S.
- [115] P. A. Redhead. *Thermal desorption of gases*. Vacuum 12(4), pp. 203 – 211, 1962. doi:10.1016/0042-207X(62)90978-8.
- [116] J. Hafner, C. Wolverton, and G. Ceder. *Toward Computational Materials Design: The Impact of Density Functional Theory on Materials Research*. MRS Bulletin 31, pp. 659–668, 2006. doi:10.1557/mrs2006.174.
- [117] P. Hohenberg and W. Kohn. *Inhomogeneous Electron Gas*. Physical Review 136, pp. B864–B871, 1964. doi:10.1103/PhysRev.136.B864.

- [118] W. Kohn and L. Sham. *Density function theory*. J. Phys. Rev. 140, pp. A1133–A1138, 1965.
- [119] R. M. Dreizler and E. K. Gross. *Density Functional Theory. An Approach to the Quantum Many-Body Problem*. Springer-Verlag Berlin Heidelberg, Berlin, Heidelberg, 1990. doi:10.1007/978-3-642-86105-5.
- [120] N. Argaman and G. Makov. *Density functional theory: An introduction*. American Journal of Physics 68(1), pp. 69–79, 2000. doi:10.1119/1.19375.
- [121] A. Groß. *Theoretical Surface Science: A Microscopic Perspective*. Springer Berlin Heidelberg, Berlin, Heidelberg, 2009. doi:10.1007/978-3-540-68969-0\_3.
- [122] J. Tersoff and D. R. Hamann. *Theory and Application for the Scanning Tunneling Microscope*. Physical Review Letters 50, pp. 1998–2001, 1983. doi:10.1103/PhysRevLett.50.1998.
- [123] J. Tersoff and D. R. Hamann. *Theory of the scanning tunneling microscope*. Physical Review B 31, pp. 805–813, 1985. doi:10.1103/PhysRevB.31.805.
- [124] J. Bardeen. *Tunnelling from a Many-Particle Point of View*. Physical Review Letters 6, pp. 57–59, 1961. doi:10.1103/PhysRevLett.6.57.
- [125] J. Zetterberg, S. Blomberg, J. Gustafson, J. Evertsson, J. Zhou, E. C. Adams, P.-A. Carlsson, M. Aldén, and E. Lundgren. *Spatially and temporally resolved gas distributions around heterogeneous catalysts using infrared planar laser-induced fluorescence*. Nature Communications 6, 2015. doi:10.1038/ncomms8076.
- [126] S. Blomberg, C. Brackmann, J. Gustafson, M. Aldén, E. Lundgren, and J. Zetterberg. *Real-Time Gas-Phase Imaging over a Pd(110) Catalyst during CO Oxidation by Means of Planar Laser-Induced Fluorescence*. ACS Catalysis 5(4), pp. 2028–2034, 2015. doi:10.1021/cs502048w.

